

The Cluster Virtual Observatory for ULF Waves

Ovidiu Dragos Constantinescu¹, Karl-Heinz Fornacon², Uwe Motschmann³, Ingo Richter⁴,
and Karl-Heinz Glassmeier¹

¹TU Braunschweig

²Technical University of Braunschweig

³Braunschweig University of Technology

⁴Technical University Braunschweig

November 24, 2022

Abstract

Since its launch in 2000, the Cluster fleet visited a vast domain of the circum-terrestrial environment, from upstream solar wind and distant tail, down to the plasmasphere, scanning in detail all magnetospheric regions during almost two solar cycles. This led to an unprecedented rich data collection of multi-point measurements which will be used for years to come to decipher the mechanisms of Solar-Terrestrial interactions.

The large volume of the data gathered by Cluster requires special strategies to make efficient use of it. To address this issue we constructed a browsable database containing ULF waves and spacecraft formation parameters. Recently, we made this database accessible at <http://plasma.space-science.ro/cluster.html>. Here we present the newly developed tool, discuss the methods used to derive the parameters and give practical examples.

The Cluster Virtual Observatory for ULF Waves

O.D. Constantinescu^{1,2}, K.H. Fornaçon¹, U. Motschmann³, I. Richter¹,
K.H. Glassmeier¹

¹Institute for Geophysics and Extraterrestrial Physics, TU Braunschweig, Germany

²Institute for Space Sciences, Bucharest, Romania

³Institute for Theoretical Physics, TU Braunschweig, Germany

Key Points:

- The Cluster Virtual Observatory is an on-line archive of low frequency wave parameters based on Cluster fluxgate magnetometers measurements.
- The Cluster Virtual Observatory also provides the tetrahedron geometrical configuration parameters.
- The waves and geometrical parameters are available as quick-plots as well as binary *Hierarchical Data Format* data.

Abstract

Since its launch in 2000, the Cluster fleet visited a vast domain of the circum-terrestrial environment, from upstream solar wind and distant tail, down to the plasmasphere, scanning in detail all magnetospheric regions during over two solar cycles. This led to an unprecedented rich data collection of multi-point measurements which will be used for years to come to decipher the mechanisms of Solar-Terrestrial interactions.

The large volume of the data gathered by Cluster requires special strategies to make efficient use of it. To address this issue we constructed a browsable database containing ULF waves and spacecraft formation parameters. Recently, we made this database accessible at <http://plasma.space-science.ro/cluster.html>. Here we present the newly developed tool, discuss the methods used to derive the parameters and give practical examples.

1 Introduction

The Cluster mission (Escoubet et al., 1997), consisting of four identical spacecraft flying in formation around the Earth, is the first multi-spacecraft mission to study the Earth's magnetosphere and the near Earth solar wind. Simultaneous measurements allowed for the first time to separate spatial from temporal fluctuations and to investigate the three-dimensional structures in the Earth's plasma environment. Each spacecraft carries 11 state-of-the-art instruments to measure the surrounding plasma properties. One of the key quantities is the magnetic field which is measured by two instruments: a searching coil magnetometer (Cornilleau-Wehrin et al., 1997) to measure high frequency fluctuations of the magnetic field and a flux gate magnetometer (FGM) (Balogh et al., 1997) to measure low frequency fluctuations. The spacecraft were launched in July and August 2000 on polar orbits and they will likely deliver science data at least until 2024 when the first spacecraft in the formation enters the Earth's upper atmosphere.

ULF waves are oscillations of the electromagnetic field occurring in the magnetised plasma around the Earth at frequencies in the order of mHz to Hz, e.g. Glassmeier (1995); Pilipenko (1990); Keiling et al. (2016). They play a crucial role in the transfer and distribution of the energy coming from the Sun by energising particles, triggering reconnection, storing and propagating energy, modifying distribution functions, and carrying information between distant regions of the magnetosphere and the solar wind. Various wave modes are excited, depending on the local plasma parameters as well as on the solar wind conditions, and each wave mode has its particular way of interacting with the magnetosphere.

Estimating the wave parameters is crucial for the wave mode identification and for understanding the part played by the waves in the Solar-Terrestrial interaction. Many of these parameters, such as the power spectral density, coherency, ellipticity, propagation direction can be determined using the magnetic field alone. Other parameters such as the Poynting vector and the phase relation between the magnetic field and the particle density, require additional measurements of other physical quantities.

Until the end of the mission, Cluster will gather the equivalent of over one century of single spacecraft data from each instrument. Managing this amount of data poses challenges in computing, storing, and searching for relevant events. For instance, only obtaining the 2000 to 2018 ULF waves parameters discussed in the following sections required more than two months of continuous computing time on the eight threads of a 3.1 GHz Intel processor. A searchable archive of pre-computed ULF waves parameters has the potential to enable event-based and statistical studies otherwise difficult to conduct.

63 The multipoint capabilities of the Cluster fleet set it apart from most other
 64 spacecraft probing the Earth’s magnetosphere and the solar wind. While even merely
 65 comparing the measurements from two spacecraft is useful in many investigations,
 66 more sophisticated techniques, such as the wave telescope / k-filtering (Motschmann
 67 et al., 1996; Pinçon & Motschmann, 1998; Glassmeier et al., 2001) or the curlometer
 68 (Dunlop et al., 2002) require specific shapes and sizes of the spacecraft formation, and
 69 their accuracy depends on the geometric parameters of the spacecraft tetrahedron.
 70 Even though computing these parameters is not as resource-demanding as computing
 71 the ULF waves parameters, a tool allowing quick estimation of the Cluster tetrahedron
 72 shape and size represents a useful instrument.

73 The remainder of this work is organized as follows: Section 2 discusses the deriva-
 74 tion of the ULF waves parameters and provides the relations used to compute them
 75 later. Similarly, section 3 discusses the tetrahedron geometric parameters. Section 4
 76 is dedicated to the Cluster Virtual Observatory and describes in detail the archived
 77 data and the capabilities of the online tool. Section 5 summarises this work.

78 2 Derivation of the ULF waves parameters

79 Among the fundamental properties of the waves in magnetized plasma are the
 80 polarization parameters: the polarization degree, the ellipticity, and the orientation of
 81 the variance ellipsoid. The first step in finding these parameters is finding the principal
 82 component system of the magnetic field. Though this can be done in various ways, the
 83 most common approach is based on the analysis of the spectral matrix obtained from
 84 the Fourier components corresponding to the analysed frequency. For the magnetic
 85 field \mathbf{B} with components B_i , $i = 1, \dots, 3$, the spectral matrix elements are:

$$86 \quad \mathcal{S}_{ij}(\omega) = \left\langle \tilde{B}_i(\omega) \tilde{B}_j^*(\omega) \right\rangle \quad i, j = 1, \dots, 3 \quad (1)$$

87 where $\langle \dots \rangle$ denotes the average and $*$ denotes the complex conjugate. The Fourier
 88 component

$$89 \quad \tilde{B}_i(\omega) = \frac{1}{2\pi} \int B_i(t) e^{-i\omega t} dt \quad (2)$$

90 is approximated by the discrete Fourier transform usually through the Fast Fourier
 91 Transform (FFT) method.

92 Arthur et al. (1976) discuss three methods which can be used to determine the
 93 polarization parameters of plasma waves. One of those was proposed by Samson
 94 (1973). This method is based on the decomposition of the spectral matrix in three
 95 terms: one corresponding to the total polarized part of the wave, one corresponding to
 96 the partial polarized part of the wave and one corresponding to the non polarized part
 97 of the wave. From this decomposition, the relative powers of the three polarization
 98 components of the wave result:

$$99 \quad P_T = \frac{\lambda_1 - \lambda_2}{\Lambda}; \quad P_P = 2 \frac{\lambda_2 - \lambda_3}{\Lambda}; \quad P_N = 3 \frac{\lambda_3}{\Lambda} \quad (3)$$

100 where $\lambda_1 \geq \lambda_2 \geq \lambda_3$ are the eigenvalues of the complex spectral matrix \mathcal{S} and $\Lambda =$
 101 $\lambda_1 + \lambda_2 + \lambda_3$. The polarization degree is given by

$$102 \quad P^2 = \frac{1}{2\Lambda} \sum_{\substack{i,j=1 \\ i < j}}^3 (\lambda_i - \lambda_j)^2 \quad (4)$$

103 This method has the advantage of decomposing the data into quantities with clear
 104 physical meaning. One drawback which could become significant in the context of
 105 processing large quantities of data is the need of solving the eigenvalue problem for a
 106 complex matrix, which is more resource demanding than for a real matrix.

107 Santolík et al. (2003) applies singular value decomposition (SVD) to the complex
 108 spectral matrix to derive many wave parameters. The SVD is much easier on resources
 109 and in addition the proposed method is generalized to naturally include the electric
 110 field vector, providing more information.

111 Other methods discard either the real or the imaginary part of the spectral
 112 matrix. An example, discussed by Arthur et al. (1976) is the direct determination of
 113 the direction of the \mathbf{k} vector from the imaginary part of the spectral matrix (Means,
 114 1972):

$$115 \hat{k}_l = \pm \Im(\mathcal{S}_{mn})/p \quad l, m, n = 1, \dots, 3; \quad l \neq n \neq m \quad (5)$$

116 where $p^2 = \sum_{i,j=1}^3 \Im(\mathcal{S}_{ij})^2$ and the sign is given by the polarization sign.

117 Once the direction of the wave vector is determined, the spectral matrix is rotated
 118 in a coordinate system with the x axis along $\hat{\mathbf{k}}$. This is relatively easy to implement
 119 numerically and requires less CPU time than needed for the diagonalization of the
 120 spectral matrix. However, since only the minimum variance direction is provided by
 121 $\hat{\mathbf{k}}$, the polarization information is incomplete. Also, purely linear polarized waves
 122 cannot be treated because in this case the spectral matrix is real.

123 The third technique considered by Arthur et al. (1976) was proposed by McPherson
 124 et al. (1972) and, in contrast with the Means (1972) method, implies the diagonal-
 125 ization of the real part of the spectral matrix. The rotation matrix \mathcal{T} can be derived
 126 from the eigenvectors of the real part of the spectral matrix $\Re(\mathcal{S})$:

$$127 \mathcal{T} = [\mathbf{v}_1, \mathbf{v}_2, \mathbf{v}_3] \quad \lambda_1 \geq \lambda_2 \geq \lambda_3 \quad (6)$$

128 The numerical implementation of the Means (1972) method is relatively straightfor-
 129 ward and no additional assumptions about the analysed waves are necessary. The
 130 spectral matrix rotated into the principal variance system becomes:

$$131 \mathcal{J} = \mathcal{T} \mathcal{S} \mathcal{T}^\dagger \quad (7)$$

132 where \dagger denotes the Hermitic conjugate (complex conjugate transpose).

133 The polarization degree is defined as the ratio between the wave coherent power
 134 and the total power of the wave (Fowler et al., 1967)

$$135 P^2 = 1 - 4 \frac{\det(\mathcal{J})}{\text{Tr}(\mathcal{J})^2} \quad (8)$$

136 For a plane wave described by

$$137 B_x(t) = b_x e^{i\omega t} \quad (9a)$$

$$138 B_y(t) = b_y e^{i\omega t - \pi/2} \quad (9b)$$

$$139 B_z(t) = b_z \quad (9c)$$

140 the spectral matrix \mathcal{J} becomes

$$142 \mathcal{J} = \begin{pmatrix} b_x^2 & ib_x b_y & 0 \\ -ib_x b_y & b_y^2 & 0 \\ 0 & 0 & 0 \end{pmatrix} \quad (10)$$

143 The ellipticity is defined as the ratio between the two axes of the polarization
 144 ellipsoid:

$$145 \epsilon = \tan \left[\frac{1}{2} \arcsin \left(\frac{2\Im(J_{xy})}{\sqrt{\text{Tr}(\mathcal{J})^2 - 4\det(\mathcal{J})}} \right) \right] \quad (11)$$

146 The orientation of the maximum variance axis is given by the azimuth angle:

$$147 \tan(2\phi) = \frac{2\Re(J_{xy})}{J_{xx} - J_{yy}} \quad (12)$$

148 The variance analysis alone only provides the direction of the wave vector up to
 149 the sign. Therefore the sign of the ellipticity in relation to the propagation direction
 150 remains undetermined as well. However, for waves in magnetized plasma, the the
 151 convention is to use the magnetic field direction instead of the propagation direction
 152 as reference for the sign of ellipticity. This is because rotations to the right or to
 153 the left with respect to the magnetic field bear the physical significance. With this
 154 convention, the sign of ellipticity is determined from the imaginary part of the spectral
 155 matrix (Means, 1972).

156 The coherency is defined using the spectral matrix elements (Rankin & Kurtz,
 157 1970):

$$158 \quad \gamma = \frac{|J_{xy}J_{yx}|}{|J_{xx}J_{yy}|} \quad (13)$$

159 while, following Song & Russell (1999), the intensity of the coherent part of the wave
 160 is

$$161 \quad I_{\text{coh}} = \lambda_1 + \lambda_2 - 2\lambda_3 \quad (14)$$

162 Any wave can be decomposed into a sum of left hand polarized and right hand
 163 polarized waves (Kodera et al., 1977) with the amplitudes given by:

$$164 \quad A_{\pm} = \frac{\sqrt{\lambda_1 - \lambda_3}}{2} (1 \pm \epsilon) \quad (15)$$

165 From these, the amplitudes of the linear polarized part of the wave and the amplitude
 166 of the circular polarized part of the wave can be determined

$$167 \quad A_{\text{lin}} = \sqrt{2A_- A_+} \quad (16)$$

$$168 \quad A_{\text{circ}} = \sqrt{|A_+^2 - A_-^2|} \quad (17)$$

170 Another important wave parameter determined using the magnetic field alone
 171 is the compression ratio, i.e. the ratio between the power spectral density of the
 172 oscillations orthogonal to the mean magnetic field (transverse power) and the total
 173 power spectral density. In a coordinate system with the z axis aligned with the mean
 174 magnetic field, the compression ratio is

$$175 \quad C = \frac{P_x + P_y}{P_x + P_y + P_z} \quad (18)$$

176 where P_j is the power spectral density of the component j . The power spectral densities
 177 for the components are determined from the diagonal elements of the spectral matrix.

178 All the parameters discussed above are derived solely from the magnetic field.
 179 However, the time varying magnetic field of the waves propagating into the plasma is
 180 coupled with the electric field, and in addition the waves also disturb and are influenced
 181 by the plasma particle distributions. To analyse the coupling between these physical
 182 quantities one must generalize the spectral matrix Eq(1) to the cross-spectral matrix
 183 of two time series, $u(t)$ and $v(t)$:

$$184 \quad \mathcal{G}_{uv}(\omega) = \langle \tilde{u}(\omega)\tilde{v}^*(\omega) \rangle \quad (19)$$

185 From the cross-spectral matrix, a number of fundamental quantities characterizing
 186 the relation between the $u(t)$ and $v(t)$ time series can be derived. One of the most
 187 important is the phase shift between u and v , for instance between the magnetic field
 188 module and the particle density:

$$189 \quad \varphi_{uv} = \arctan(\mathcal{G}_{uv}) \quad (20)$$

The coherency between $u(t)$ and $v(t)$ gives the similarity degree of two time series. The more stable the phase difference and the amplitude ratio of two signals are, the more coherent they are.

$$\gamma_{uv}(\omega) = \frac{|\mathcal{G}_{uv}|^2}{\mathcal{G}_{uu}\mathcal{G}_{vv}} \quad (21)$$

For a single time series, the coherency Eq. (13) is a particular case Eq. (21).

The co-spectrum, equal to the real part of the extra-diagonal elements, $\Re(\mathcal{G}_{uv})$, represents the in-phase and opposite-phase part of the signals. The quad-spectrum, equal to the imaginary part of the extra-diagonal elements, $\Im(\mathcal{G}_{uv})$, represents phase-quadrature ($\pm\pi/2$ phase difference, advanced/retarded) part of the signals.

Finally, a key parameter of the ULF waves is the Poynting vector which provides the electromagnetic energy flux:

$$\mathbf{S}(\omega) = \frac{1}{2\mu_0} \Re(\tilde{\mathbf{E}} \times \tilde{\mathbf{B}}^*) \quad (22)$$

Knowledge of the Poynting vector supports the identification of stationary waves, and of energy source and sink regions.

3 Derivation of the geometric parameters

All multipoint data analysing techniques depend on the geometric properties of the sensor network. The minimum number of measuring points required for deriving three dimensional quantities and to differentiate between spatial and temporal fluctuations is four, the number of spacecraft in the Cluster fleet. However, not any configuration of four spacecraft is appropriate for three dimensional analysis. The dimensionality is reduced to 2 if all spacecraft are contained in a plane and to 1 if they are aligned along a line. To characterize the configurations lying in between these extremes one may use the elongation and planarity parameters derived from the volumetric tensor which is defined as (Robert, Roux, et al., 1998):

$$R_{ij} = \frac{1}{N} \sum_{\alpha=1}^N r_i^\alpha r_j^\alpha \quad (23)$$

where r_k^α is the component k of the position vector \mathbf{r}^α of spacecraft α relative to the baricenter of the formation, $\sum_{\alpha=1}^N \mathbf{r}^\alpha = 0$.

The characteristic dimensions of the tetrahedron are given by the eigenvalues of the volumetric tensor \mathcal{R} , while the eigenvectors give the orientation of the volumetric ellipsoid. For Cluster, $N = 4$ and the volume of the tetrahedron is given by the determinant of the volumetric tensor $V = (8/3)\sqrt{|\mathcal{R}|}$. Therefore when $|\mathcal{R}| = 0$, the formation is either flattened into a 2D plane or elongated into a 1D line.

If $a_1 \geq a_2 \geq a_3$ are the eigenvalues, and $\mathbf{R}_1, \mathbf{R}_2, \mathbf{R}_3$ are the corresponding eigenvectors of the volumetric tensor \mathcal{R} , the elongation is defined as

$$e = 1 - \sqrt{\frac{a_2}{a_1}} \quad (24)$$

with the direction given by the eigenvector \mathbf{R}_1 corresponding to the maximum eigenvalue. When the elongation approaches 0, the spacecraft tend to be equally distanced from each other, when the elongation approaches 1, the tetrahedron shape degenerates to a string.

The planarity is defined as

$$p = 1 - \sqrt{\frac{a_3}{a_2}} \quad (25)$$

with the normal to the flattening given by the eigenvector \mathbf{R}_3 corresponding to the minimum eigenvalue. When the planarity approaches 1, all spacecraft are contained in a plane.

The pair (e, p) gives the shape of the formation and determines its dimensionality which is of key importance for multi-spacecraft analysis methods.

The size of the constellation also matters. The characteristic size of the tetrahedron is the largest dimension of the volumetric ellipsoid

$$L = 2\sqrt{a_1} \quad (26)$$

If the distances between the spacecraft are larger than the correlation length of the phenomenon being studied, then the measurements become just a collection of unrelated single point measurements and can be combined only in a statistical sense. Within the correlation length, if the distances between spacecraft are larger than the wavelength / scale of the phenomenon being investigated, spatial aliasing will occur (Sahraoui et al., 2010). If the distances between the spacecraft become too small compared with the scale of the phenomenon being studied, then the measurements become identical and the constellation becomes equivalent with a single point measurement.

4 The online virtual observatory

The almost two solar cycles covered by Cluster multipoint magnetospheric measurements are a valuable resource offering opportunities for unprecedented statistical studies, as well as for case studies of common phenomena in extreme or unusual conditions. For the study of plasma waves over individual time intervals one could use dedicated analysing tools such as PRASSADCO (Cornilleau-Wehrin et al., 2005) to compute and visualize the key waves parameters. However, the sheer size of the data collected by Cluster over two decades poses new challenges in managing and filtering the data. This is why a database containing high level data is essential to make these studies possible. The more resource-demanding the computation of the high level data is, the more valuable the database becomes. The parameters of the ULF waves discussed in Sec. 2 are among the best candidates for such database.

To take full advantage of the multipoint measurements offered by Cluster, one must employ specialised multipoint techniques, such as the curlometer (Robert, Dunlop, et al., 1998; Dunlop et al., 2002) or the wave telescope (Glassmeier et al., 2001) which work only for specific geometric configurations of the Cluster tetrahedron. A database allowing quick retrieval of these parameters can substantially ease the search for (or confirmation of) suitable configurations.

The magnetic field data used to compute the ULF waves parameters is obtained by calibrating locally stored level0 FGM data using daily calibration parameters produced by the TUBS team. Other data such as the electric field and the particle density are obtained from the ESA *Cluster Science Archive* (<https://cosmos.esa.int/web/csa>).

4.1 ULF waves parameters

Using measurements of the magnetic field \mathbf{B} , electric field \mathbf{E} and the spacecraft potential (to derive the electron density n (Lybekk et al., 2012)), 47 parameters characterising the ULF waves are computed, saved in the database and plotted to enable quick browsing. A list of the computed parameters can be found in the *Supporting Information*.

Before computing the ULF waves parameters, the magnetic field data is pre-processed to identify data gaps and bad data, and resampled to one vector per second rate.

When available, high resolution (25 or 450 vect/s) electric field data are downloaded from the CSA. These are also resampled to one vector per second and synchronized with the magnetic field data. For the time intervals without high resolution electric field data available, low resolution (one vector per 4 seconds) are used. In this case the resulting frequency domain is more restricted. The electron density is obtained from the spacecraft potential following Lybekk et al. (2012). The advantage over using the density delivered by the dedicated particle instruments is the much higher temporal resolution and data availability.

The computed parameters are valid only under certain conditions. For instance, all the parameters involving the magnetic field lose their validity when the magnetic field variations decrease towards the noise level. A binary mask based on the power spectral density is constructed to mark the invalid time-frequency regions. Similarly, binary masks are constructed based on the PSDs of the electric field and of the Poynting vector, on the polarization degree, on the spectral matrix eigenvalues ratio, on the coherency between the magnetic field and the density variations, and on the angle between the wave vector and the mean magnetic field direction. Not all masks are applied to all parameters, for instance, the last mask ($\widehat{k\mathbf{B}}$) is only used to mark as bad the computed ellipticity when the wave vector is nearly parallel to the mean magnetic field. The masks are saved together with the computed parameters and are used to remove the bad values from the plots.

4.1.1 Plots archive

The heart of the ULF Observatory is the browsable archive of plots representing the wave parameters as daily spectrograms. While all parameters enumerated in Sec. 4.1 are saved in the data archive, only a subset of them are part of the plots archive. The plots are organized into six sets of seven parameters each. To facilitate visual analysis, the first panel for all plot sets shows the time series of the magnetic field together with condensed information about the orbit. In addition, the magnetospheric regions crossed by the spacecraft and the location of the magnetic foot points when the spacecraft orbit intersects closed field lines are encoded by horizontal coloured bars. The information about the magnetospheric regions and foot points is obtained from the Goddard SSCWeb interface <http://sscweb.gsfc.nasa.gov> using IGRF internal and Tsyganenko 89C external model and is only meant as a rough guide. Many parameters appear in multiple sets, therefore the total number of distinct parameters in the plots archive is 29. We briefly describe below the default parameter set in the plots archive. The other five sets are shown and discussed in the *Supporting Information*.

The basic parameters set is illustrated in Fig. 1. The top panel shows the time series for the three components of the magnetic field in GSE coordinates. The plotted magnetic field is high-pass filtered to exclude periods larger than one hour. To differentiate between the three components, an offset of 5 nT is added to the x component and subtracted from the y component. The three insets on the left show the projections of the spacecraft orbit on the GSE (x,z) , (y,z) and (x,y) planes with the starting point marked by the magenta circle. The coloured bar at the top of the panel indicates the magnetospheric regions crossed by the spacecraft according to Tsyganenko 89C (Tsyganenko, 1989) with $K_p = 3$, in this case dayside magnetosheath during the entire interval. Because of departures of the actual K_p index from the constant index used, and because of the dynamics of the magnetospheric boundaries, one can clearly see from the data that in fact the spacecraft finds itself in the solar wind at the beginning of the interval and the bowshock moves back and forth several times until the spacecraft moves deeper into the magnetosheath. If the spacecraft reaches further into the magnetosphere into the closed field lines region, then the foot points in the northern and southern hemisphere would be indicated by two coloured bars stacked

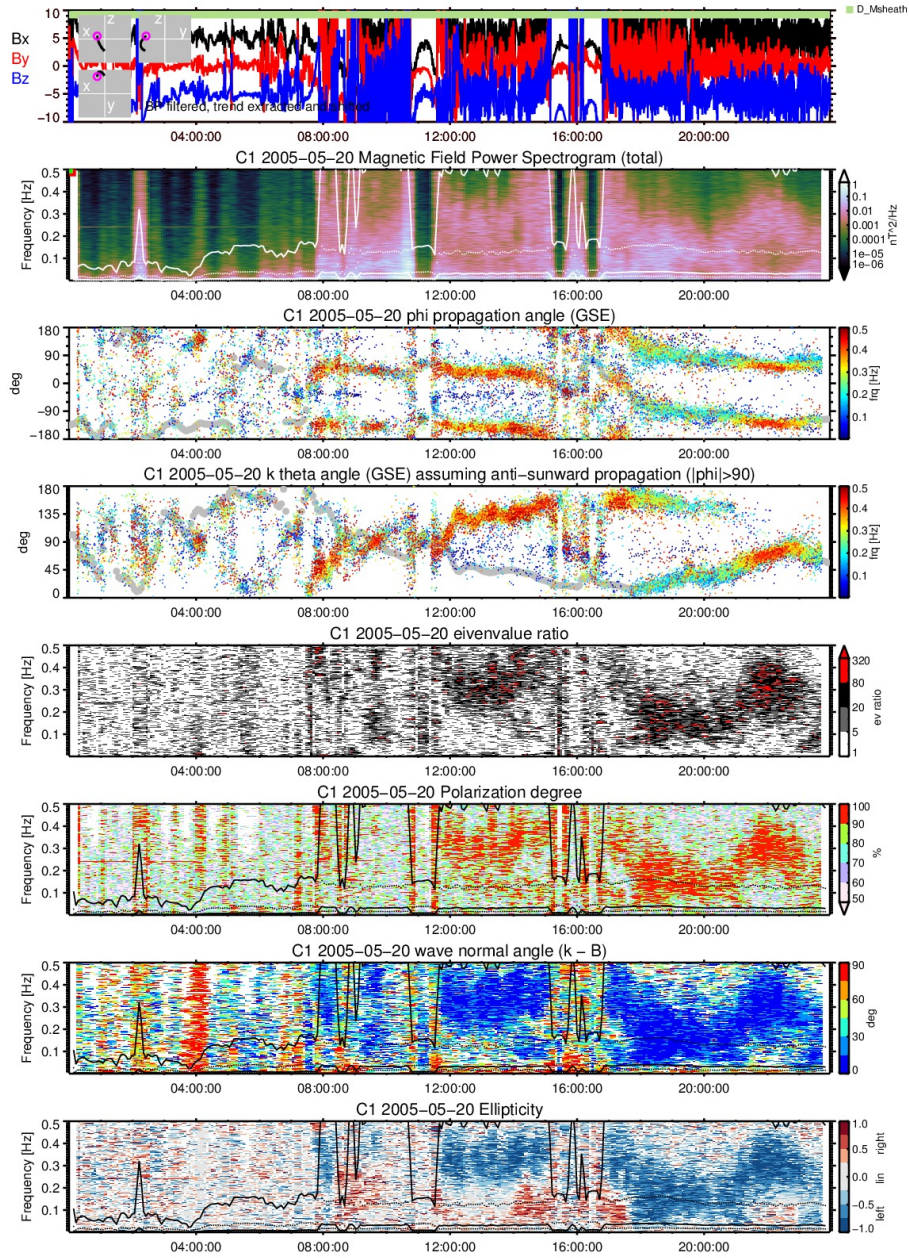


Figure 1. The *basic parameters* plot set for C1 on 20th May 2005. From top to bottom: GSE components of the magnetic field, HP filtered. The insets show the orbit in GSE, the top bar shows the magnetospheric region; Sum of the PSD of the magnetic field components. The white lines show the gyrofrequencies of H, He, and O; Azimuth and elevation directions of the wave vector in GSE; Colour encodes the frequency, grey thick line shows the mean field direction; Ratio between intermediate and minimum eigenvalue; Polarization degree; Angle between wave vector and mean field; Ellipticity.

329 at the bottom of the panel, not present in this figure, but visible in Fig. S10 showing
330 the web interface.

331 The first parameter in the set is the total power spectral density of the magnetic
332 field fluctuations, defined as the sum of the power spectral densities of the three GSE
333 components computed – as all other parameters – using 1 s resolution data and a
334 sliding window W of 2048 s with a step Δt of 256 s. The PSD per Hz per s in the
335 time-frequency cell ($\nu - \Delta\nu/2$ to $\nu + \Delta\nu/2$, $t - \Delta t/2$ to $t + \Delta t/2$) for the component
336 j is computed as

$$337 \quad P_j(\nu, t) = 2W \left| \tilde{B}_j(\nu) \right|^2 \Bigg|_{t-\frac{W}{2}}^{t+\frac{W}{2}} \quad (27)$$

338 where W is the window length in seconds, $\Delta\nu = 1/W$ is the FFT frequency resolution
339 in Hz, Δt is the sliding step in seconds and $\tilde{B}_j(\nu)$ is the Fourier transform Eq. (2) of
340 the magnetic field evaluated in the time interval $(t - W/2, t + W/2)$. The total wave
341 energy contained in the $(\Delta\nu, \Delta t)$ cell is equal with the PSD multiplied by the cell area,
342 $\Delta\nu\Delta t$: $E_{\text{cell}}(\nu, t) = 2\Delta t |\tilde{B}_j(\nu, t)|^2$.

343 The gyrofrequencies of the H, He and O computed from the magnetic field
344 smoothed using a boxcar average of 1024 s are plotted on top of the spectrogram
345 with white solid, dotted and again solid lines, respectively. The position of the space-
346 craft relative to the GSE (x, y) (equatorial) and (x, z) (noon-midnight meridian plane)
347 planes is marked at the top of this panel by coloured bars as follows: Red if the angle
348 between the position vector and the equatorial plane is less than 10° . Yellow if the
349 angle between the position vector and the noon-midnight meridian plane is less than
350 10° and the x coordinate is positive (dayside). Green if the angle between the position
351 vector and the noon-midnight meridian plane is less than 10° and the x coordinate is
352 negative (nightside). None of these conditions occurred during 20th May 2005 there-
353 fore no coloured bars are present in Fig. 1 PSD panel. Fig. S10 shows an example when
354 the spacecraft orbit intersects both planes.

355 The next two panels show the orientation of the wave vector \mathbf{k} Eq. (5) as given by
356 the azimuth φ and by the elevation θ angles in GSE coordinates. The corresponding
357 frequencies are colour coded. In both panels the mean magnetic field direction is
358 represented with a thick grey line in the background. Because of the uncertainty
359 in the sign of \mathbf{k} , frequent jumps between opposite directions of the \mathbf{k} vector can be
360 noticed in the azimuth angle. We could have limited the representation to half-space
361 without losing any information, however, in order to show the mean field direction
362 together with the wave vector we choose to represent the entire space. Nevertheless,
363 we changed the elevation angle to correspond to anti-sunward propagation ($|\varphi| \leq 90$).
364 With this convention inside the magnetosheath the waves propagate anti-parallel to
365 the magnetic field at the beginning and parallel to the magnetic field towards the end.
366 Outside the magnetosheath the propagation direction is less well defined. During this
367 day the wave propagation direction does not depend on frequency.

368 To remove from the plot low power fluctuations we discarded the time-frequency
369 cells corresponding to total PSD less than $10^{-3} \text{ nT}^2 \text{ Hz}^{-1} \text{ s}^{-1}$. We applied this power
370 mask to all parameters derived from the magnetic field, except the other power spectral
371 densities. Moreover, to reduce the noise in the plot we discarded the time-frequency
372 cells corresponding to polarization degree below 70%. Finally, because a low eigenvalue
373 ratio leads to large errors in the determined wave vector direction we also discarded
374 the time-frequency cells corresponding to eigenvalue ratios less than 5.

375 The ratio between the intermediate and the minimum eigenvalues of the spectral
376 matrix Eq. (1) plotted in the next panel provides useful information about how well the
377 wave propagation direction is defined. To properly represent the range of eigenvalue
378 ratios we use a logarithmic base 4 representation. All cells below the threshold ratio

379 (equal to 5) are masked out (white) and all values above 80 are plotted with red. Other
380 masks applied: PSD.

381 The polarization degree Eq. (8) is shown in the next panel. Only the PSD mask
382 is applied here. Note that the high polarization domain resembles the large eigenvalue
383 ratio domain in the previous panel. Here and in the next two panels the gyrofrequencies
384 of H, He and O are plotted with black lines on top of the spectrogram.

385 The penultimate panel shows the wave normal angle, i.e. the angle between
386 the wave vector and the mean magnetic field computed over the window length W .
387 Because of the sign uncertainty we reduced the angles to the $[0^\circ, 90^\circ]$ interval. For this
388 panel we applied the masks for PSD, polarization degree and eigenvalue ratios with the
389 thresholds mentioned above. One can see that during this day most of the waves with
390 high polarization and power in the magnetosheath propagate either parallel or anti-
391 parallel to the mean magnetic field. In front of the magnetosheath the waves do not
392 seem to have a preferred direction with the exception of a short time interval around
393 04 UT when the wave vector is orthogonal to the magnetic field for all frequencies.

394 The last panel in this set shows the waves ellipticity Eq. (11). For this panel
395 we applied the same masks as for the wave normal angle. In addition we masked out
396 the time-frequency cells with near orthogonal propagation ($\alpha_{kB} \geq 80^\circ$) because for
397 orthogonal propagation the ellipticity is undefined. Most of the parallel propagating
398 waves are circularly polarized to the left with some exceptions in the lower frequency
399 range close to the bowshock crossings when the polarization is to the right. In front
400 of the bowshock no preferred ellipticity is observed with the exception of the waves
401 around 04 UT showing linear polarization.

402 **4.1.2 Data archive**

403 The daily 330×1025 time-frequency matrix for each parameter is saved using
404 the *Hierarchical Data Format* (HDF) standard (Poinot, 2010), together with a low
405 resolution plot for quick reference. The corresponding time and frequency vectors,
406 details on how the parameter was computed, the reference system, and the units used
407 are saved as well in the same HDF file. The total size of the archived parameters is
408 over 2 TB. This high level database can be used to automatically search for events
409 satisfying certain imposed conditions for case or statistical studies.

410 A subset of the low resolution plots meant for quick visual inspection of the
411 database content are presented in the *Supporting Information*. To avoid obscuring po-
412 tential significant features, no masks are applied, therefore one should exercise caution
413 when interpreting these plots.

414 **4.2 Geometric parameters**

415 The geometric parameters characterize the shape and the size of the Cluster
416 tetrahedron. They are essential for determining the applicability and for the error
417 evaluation of multi-point analysis techniques. In Sec. 3 we introduced the elongation
418 and the planarity which condense the shape information for a tetrahedron in an in-
419 tuitive fashion. Since both can only take values between 0 and 1, any tetrahedron
420 shape corresponds to one point in the unit square of the elongation-planarity diagram.
421 Table 1 summarises the possible shapes in the (e,p) space.

422 For a long term overview of the geometric parameters of the Cluster tetrahedron
423 we produced plots such as the one shown in Fig. 2. Each plot consists of four panels,
424 each panel showing the mean inter-spacecraft distance during one year. The shape of
425 the formation is encoded in the colour of the plot line, with a colour-key in the upper
426 right corner. The colour-key is a representation of the (e,p) space, with the origin

Table 1. Shapes in the planarity-ellipticity domain. Adapted from Robert, Roux, et al. (1998).

p \ e	0	low	intermediate	large	1
1	circle	ellipse			
large	ellipsoid	pancake	elongated pancake	knife blade	
intermediate		thick pancake	potato	flat cigar	
low	pseudo sphere	short cigar	cigar		
0	sphere	rugby ball			

427 $(0, 0)$ at the lower left corner, and maximum value $(1, 1)$ at the upper right corner.
 428 The red colour near origin indicates a nearly regular tetrahedron. The yellow colour
 429 (large elongation, low planarity) indicates cigar shapes. The green colour indicates
 430 shapes resembling a long, flat knife blade. The blue colour indicates nearly circular
 431 flattened pancake shaped formations. The grey colour in the centre indicates irregular
 432 “potato” shapes. The function chosen to map the (e, p) space to the (r, g, b) space is
 433 bijective, therefore one can estimate the shape of the tetrahedron at a given moment
 434 in time from the colour of the corresponding line in the plot.

435 Yearly, monthly and daily plots are also provided. Detailed descriptions and
 436 example plots are included in the *Supporting Information*.

437 4.3 The web interface

438 The Cluster virtual observatory for ULF waves is organized into three main
 439 sections. The *ULF quickplots* (Fig. S10, <http://plasma.space.science.ro/waves/index.html>)
 440 section offers access to the plots archive discussed in sec. 4.1.1. The
 441 spacecraft, date, and plot set can be selected using the buttons above the image.
 442 Below the image, there are links to high resolution JPG or pdf formats of the plots,
 443 to a catalogue containing the plots for the entire year, and to a text file with details
 444 about how the plots were produced. This text file is embedded both in the JPG image
 445 header and in the pdf file.

446 The *ULF data* (Fig. S11, <http://plasma.space.science.ro/waves/spectra-data/>)
 447 section offers access to the ULF waves parameters data archive discussed in sec. 4.1.2.
 448 The spacecraft, year, month and parameter are selected using the buttons at the top
 449 of the page. The “go” button displays the low resolution images of the selected pa-
 450 rameter for the selected month together with links to the HDF files containing the
 451 archived data.

452 The *Tetrahedron geometry* (Fig. S12, <http://plasma.space.science.ro/waves/geometry.html>)
 453 section offers access to the plots of the geometric parameters of the
 454 Cluster fleet discussed in sec. 4.2. From the buttons at the top of the page, the desired
 455 plot can be selected and displayed. Links to high resolution JPG and pdf files as well
 456 as to a yearly catalogue are provided at the bottom of the page.

457 5 Summary and conclusions

458 The large volume of data accumulated by the Cluster mission in the last two
 459 decades is both a valuable resource and a challenge to digest in an efficient manner.
 460 The many parameters characterizing the low frequency plasma waves are a good ex-
 461 ample of high level data whose availability have the potential to significantly reduce
 462 the effort needed to select relevant events or to conduct large statistical studies. If
 463 multipoint analyses are performed, a possibility to quickly find appropriate spacecraft

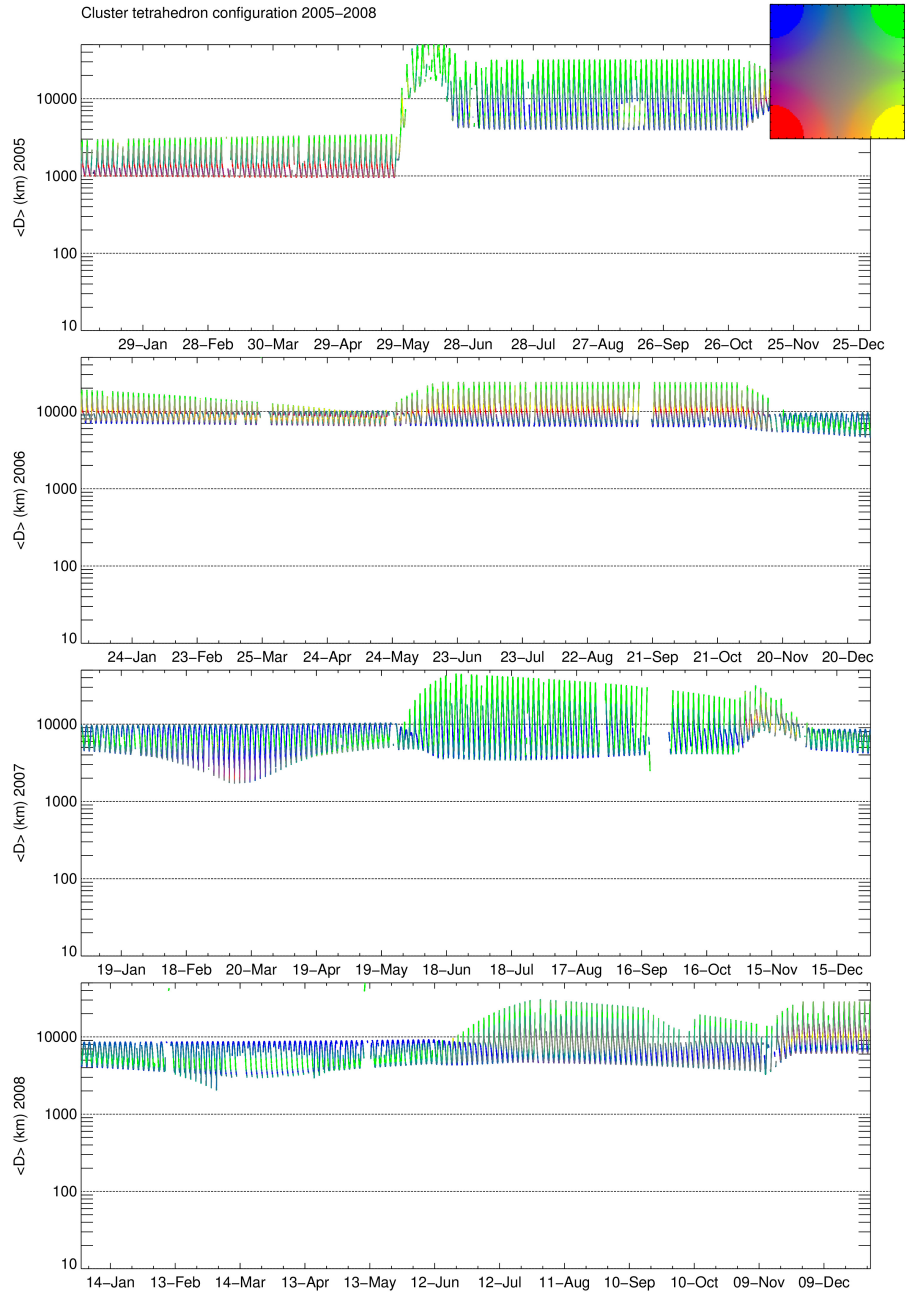


Figure 2. Geometric parameters of the Cluster tetrahedron between 2005 and 2008. The y axis shows the mean inter-spacecraft distance and the colour encodes the tetrahedron shape in the (e,p) domain as given by the colour legend in the upper right.

464 configurations is highly desirable as well. The Cluster Virtual Observatory (CVO)
 465 offers both the high level ULF waves parameters and an optimized interface to graphi-
 466 cal representations of the spacecraft configuration. A browsable database of daily
 467 plots of the ULF waves parameters allows for a rapid search for significant events and
 468 provides publication quality images. The main data used to build the CVO database
 469 is the magnetic field delivered by the Cluster FGM instruments. Additionally, the
 470 spacecraft potential and the electric field from the EFW instrument are used to com-
 471 pute specific parameters. For a rough positioning within the magnetospheric regions,
 472 data from the Goddard SSCWeb is utilised. The Cluster Virtual Observatory can be
 473 accessed without restrictions at <http://plasma.space-science.ro/cluster.html>.

474 Acknowledgments

475 This work was financially supported by the Deutsches Zentrum für Luft- und
 476 Raumfahrt under contract 50OC1803. The *ULF quick plots* and *ULF data* sections
 477 of the CVO until 2018 were supported by the Romanian Space Agency STAR pro-
 478 gram, Contract 149/20.07.2017. Datasets for this work are available from the ESA
 479 *Cluster Science Archive* (<https://cosmos.esa.int/web/csa>) and from the Goddard
 480 SSCWeb interface (<http://sscweb.gsfc.nasa.gov>).

481 References

- 482 Arthur, C. W., McPherron, R. L., & Means, J. D. (1976). A comparative study
 483 of three techniques for using the spectral matrix in wave analysis. *Radio Science*,
 484 *11*(10), 833–845. doi: 10.1029/RS011i010p00833
- 485 Balogh, A., Dunlop, M. W., Cowley, S. W. H., Southwood, D. J., Thomlinson, J. G.,
 486 Glassmeier, K. H., ... Kivelson, M. G. (1997, January). The Cluster Magnetic
 487 Field Investigation. *Space Science Reviews*, *79*, 65–91.
- 488 Cornilleau-Wehrlin, N., Chauveau, P., Louis, S., Meyer, A., Nappa, J. M., Perraut,
 489 S., ... Louarn, P. (1997, January). The Cluster Spatio-Temporal Analysis of Field
 490 Fluctuations (STAFF) Experiment. *Space Science Reviews*, *79*, 107–136.
- 491 Cornilleau-Wehrlin, N., Alleyne, H. S., Yearby, K. H., de la Porte de Vaux, B.,
 492 Meyer, A., Santolík, O., ... Cao, J. (2005). The staff-dwp wave instrument on
 493 the dsp equatorial spacecraft: description and first results. *Annales Geophysicae*,
 494 *23*(8), 2785–2801. doi: 10.5194/angeo-23-2785-2005
- 495 Dunlop, M. W., Balogh, A., Glassmeier, K. H., & Robert, P. (2002, November).
 496 Four-point Cluster application of magnetic field analysis tools: The Curlometer. *J.*
 497 *Geophys. Res. Space Phys.*, *107*(A11), 1384. doi: 10.1029/2001JA005088
- 498 Escoubet, C. P., Schmidt, R., & Goldstein, M. L. (1997). Cluster: Science and Mis-
 499 sion Overview. *Space Sci. Rev.*, *79*, 11–32.
- 500 Fowler, R., Kotick, B., & Elliott, R. (1967). Polarization Analysis of Natural and
 501 Artificially Induced Geomagnetic Microplulsations. *J. Geophys. Res.*, *72*, 2871–
 502 2883.
- 503 Glassmeier, K.-H. (1995). ULF pulsations. In H. Volland (Ed.), *Handbook of atmo-*
 504 *spheric electrodynamics* (p. 463–502). CRC Press.
- 505 Glassmeier, K.-H., Motschmann, U., Dunlop, M., Balogh, A., Acuña, M. H., Carr,
 506 C., ... Buchert, S. (2001). Cluster as a wave telescope - first results from the
 507 fluxgate magnetometer. *Ann. Geophys.*, *19*, 1439–1447. (Correction, *Annales*
 508 *Geophysicae*, *21*, 1071, 2003)
- 509 Keiling, A., Lee, D., & Nakariakov, V. (Eds.). (2016). *Low frequency waves in space*
 510 *plasmas*. American Geophysical Union. doi: 10.1002/9781119055006
- 511 Kodera, K., Gendrin, R., & de Villedary, C. (1977, Mar). Complex representation
 512 of a polarized signal and its application to the analysis of ULF waves. *J. Geophys.*
 513 *Res.*, *82*(7), 1245. doi: 10.1029/JA082i007p01245

- 514 Lybekk, B., Pedersen, A., Haaland, S., Svenes, K., Fazakerley, A. N., Masson, A.,
515 ... Trotignon, J.-G. (2012, January). Solar cycle variations of the Cluster space-
516 craft potential and its use for electron density estimations. *Journal of Geophysical*
517 *Research (Space Physics)*, *117*, A01217. doi: 10.1029/2011JA016969
- 518 McPherron, R. L., Russell, C. T., & Coleman, P. J., Jr. (1972, July). Fluctuating
519 Magnetic Fields in the Magnetosphere. II: ULF Waves. *Space Sci. Rev.*, *13*, 411-
520 454. doi: 10.1007/BF00219165
- 521 Means, J. D. (1972, October). Use of the three-dimensional covariance matrix in
522 analyzing the polarization properties of plane waves. *J. Geophys. Res.*, *77*, 5551-
523 5559. doi: 10.1029/JA077i028p05551
- 524 Motschmann, U., Woodward, T. I., Glassmeier, K. H., Southwood, D. J., & Pinçon,
525 J. L. (1996, March). Wavelength and direction filtering by magnetic measurements
526 at satellite arrays: Generalized minimum variance analysis. *J. Geophys. Res.*, *101*,
527 4961-4966.
- 528 Pilipenko, V. A. (1990, December). ULF waves on the ground and in space.
529 *Journal of Atmospheric and Terrestrial Physics*, *52*, 1193-1209. doi: 10.1016/
530 0021-9169(90)90087-4
- 531 Pinçon, J., & Motschmann, U. (1998). Multi-Spacecraft Filtering: General Frame-
532 work. In G. Paschmann & P. Daly (Eds.), *Analysis methods for multi-spacecraft*
533 *data* (p. 65-78). Bern: ISSI.
- 534 Poinot, M. (2010, September). Five Good Reasons to Use the Hierarchical Data For-
535 mat. *Computing in Science and Engineering*, *12*(5), 84-90. doi: 10.1109/MCSE
536 .2010.107
- 537 Rankin, D., & Kurtz, R. (1970, Oct). Statistical study of micropulsation polariza-
538 tions. *J. Geophys. Res.*, *75*(28), 5444-5458. doi: 10.1029/JA075i028p05444
- 539 Robert, P., Dunlop, M. W., Roux, A., & Chanteur, G. (1998, January). Accuracy of
540 Current Density Determination. *ISSI Scientific Reports Series*, *1*, 395-418.
- 541 Robert, P., Roux, A., Harvey, C. C., Dunlop, M. W., Daly, P. W., & Glassmeier,
542 K.-H. (1998, January). Tetrahedron Geometric Factors. *ISSI Scientific Reports*
543 *Series*, *1*, 323-348.
- 544 Sahraoui, F., Belmont, G., Goldstein, M. L., & Rezeau, L. (2010, April). Limitations
545 of multispacecraft data techniques in measuring wave number spectra of space
546 plasma turbulence. *Journal of Geophysical Research (Space Physics)*, *115*(A4),
547 A04206. doi: 10.1029/2009JA014724
- 548 Samson, J. C. (1973, December). Descriptions of the Polarization States of Vec-
549 tor Processes: Applications to ULF Magnetic Fields. *Geophysical Journal Interna-*
550 *tional*, *34*, 403-419. doi: 10.1111/j.1365-246X.1973.tb02404.x
- 551 Santolík, O., Parrot, M., & Lefeuvre, F. (2003, February). Singular value decompo-
552 sition methods for wave propagation analysis. *Radio Science*, *38*(1), 1010. doi: 10
553 .1029/2000RS002523
- 554 Song, P., & Russell, C. T. (1999, January). Time Series Data Analyses in Space
555 Physics. *Space Sci. Rev.*, *87*, 387-463. doi: 10.1023/A:1005035800454
- 556 Tsyganenko, N. A. (1989, January). A magnetospheric magnetic field model with
557 a warped tail current sheet. *Planet. Space Sci.*, *37*(1), 5-20. doi: 10.1016/0032
558 -0633(89)90066-4

Supporting Information for ”The Cluster Virtual Observatory for ULF Waves”

O.D. Constantinescu^{1,2}, K.H. Fornaçon¹, U. Motschmann³, I. Richter¹,

K.H. Glassmeier¹

¹Institute for Geophysics and Extraterrestrial Physics, TU Braunschweig, Germany

²Institute for Space Sciences, Bucharest, Romania

³Institute for Theoretical Physics, TU Braunschweig, Germany

Contents of this file

1. List of the ULF parameters available through the CVO
2. Description of the wave vector direction set
3. Description of the B MFA set
4. Description of the B – density set
5. Description of the Poynting vector direction set
6. Description of the Poynting vector MFA set
7. Description of the low resolution plots
8. Description of the yearly, monthly and daily configuration plots
9. Figure S1: Wave vector direction set

Corresponding author: O. D. Constantinescu, Institute for Geophysics and Extraterrestrial Physics, TU Braunschweig, Germany (d.constantinescu@tu-bs.de)

10. Figure S2: M MFA set
11. Figure S3: B - density set
12. Figure S4: Poynting vector direction set
13. Figure S5: Poynting vector MFA set
14. Figure S6: Yearly configuration plot
15. Figure S7: Monthly configuration plot
16. Figure S8: Daily configuration plot
17. Figure S10: ULF parameters plots CVO web page
18. Figure S11: ULF parameters data CVO web page
19. Figure S12: Tetrahedron configuration plots CVO web page

Introduction

Here we list all the waves and geometric configuration parameters made available through the CVO and we present examples of plots archive and screenshots of the CVO web interface.

All the parameters are computed in the time frequency domain using (directly or indirectly) a sliding window of 2048 s (34 min and 8 s). The sliding step of 256 s (4 min and 16 s) is one eighth of the window length. For a 24 h interval, 330 evaluations are thus performed on the time axis. A sample rate of one second results in a Nyquist frequency of 0.5 Hz. The frequency resolution from the *Fast Fourier Transform* (FFT) method is equal to the inverse of the window length (1.025 mHz), while the number of frequencies for which each parameter is computed is equal to half of the window size plus one (1025 frequencies). Therefore, for one day interval of data, each parameter is computed for

each cell of a 330×1025 domain in the time-frequency space. To reduce the statistical fluctuations a 5 points boxcar (two points to the left and two points to the right) average over frequency domain is performed for all parameters.

List of ULF parameters available through the CVO

The parameters can be grouped as follows:

- parameters derived from a single physical quantity

- ★ Power spectral densities (PSD)

- magnetic field (**B**)

- ▷ PSD of the coherent part

- ▷ PSD of distinct components

- x, y, z in the GSE coordinate system

- orthogonal and parallel components in the MFA coordinate system

- ▷ PSD corresponding to distinct polarization modes

- linear polarized

- circular polarized

- right hand polarized

- left hand polarized

- electric field (**E**)

- ▷ total Power spectral density (sum of the PSDs of the three components)

- electron density (n)

- ▷ Power spectral density of the electron density fluctuations

- ★ polarization parameters (**B**)

- coherency between the two principal components
- compression ratio
- ellipticity
- ratio between the intermediate and minimum eigenvalues
- polarization degree
- ★ directions obtained from magnetic field variance analysis (**B**)
 - angle between the wave vector and the mean magnetic field direction
 - angle between the wave vector and the poloidal direction in SM coordinates
 - angle between the wave vector and the radial direction in SM coordinates
 - angle between the wave vector and the toroidal direction in SM coordinates
 - azimuth angle of the wave vector in GSE coordinate system
 - elevation angle of the wave vector in GSE coordinate system
 - azimuth angle of the maximum variance direction in GSE
 - elevation angle of the maximum variance direction in GSE
- parameters derived from more physical quantities
 - ★ magnetic field - electron density (B, n)
 - coherency between the magnetic field and density variations
 - phase shift between the magnetic field module and density variations
 - co-spectrum between the magnetic field module and density variations
 - quad-spectrum between the magnetic field module and density variations
 - ★ magnetic field - electric field (**B, E**)
 - Poynting vector module (S)

- components of the Poynting vector (\mathbf{S})
 - ▷ x, y, z in GSE coordinate system
 - ▷ parallel and orthogonal components on the mean \mathbf{B}
- direction of the Poynting vector
 - ▷ angle between the Poynting vector and the wave vector
 - ▷ angle between the Poynting vector and the mean magnetic field
 - ▷ angle between the Poynting vector and the poloidal direction in SM
 - ▷ angle between the Poynting vector and the radial direction in SM
 - ▷ angle between the Poynting vector and the toroidal direction in SM
 - ▷ azimuth angle of the Poynting vector in GSE
 - ▷ elevation angle of the Poynting vector in GSE

Description of the wave vector direction set

The first and the last two panels in this set illustrated in Fig. S1 are the same with the corresponding ones in the *Basic parameters* set. The total PSD is replaced in the second panel by the PSD of the coherent part of the fluctuations computed from the coherent intensity Eq. (14): $P_{\text{coh}} = 2WI_{\text{coh}}$.

The two panels in the third row show the direction of the wave vector as scatter plots in the (θ, φ) domain. The time is colour coded. The directions corresponding to 30° cones around the positive and negative directions of the coordinate system axes are plotted as ellipses for the x and y axes and as horizontal lines for the z axis. The coordinate system used for the left hand side panel is a Local Magnetic Coordinate (LMC) system defined starting from the position vector of the spacecraft in the Solar Magnetic (SM) coordinate system (Laundal & Richmond, 2017): The z axis is defined as the geocentric

radial direction, the y axis is defined by the cross product of the z axis of the SM coordinate system and the radial direction: $\hat{e}'_y = \hat{e}_z^{\text{SM}} \times \hat{e}'_z / |\hat{e}_z^{\text{SM}} \times \hat{e}'_z|$. This axis points eastward in the toroidal direction. The x axis completes the right handed system and points southward in the poloidal direction: $\hat{e}'_x = \hat{e}'_y \times \hat{e}'_z$. The LMC system is useful in the inner magnetosphere where the dipole field dominates. The right hand side panel uses the GSE coordinate system with the x axis pointed towards the Sun and the y axis in the ecliptic plane. In accord with the conclusions drawn from the previous plot set, the propagation direction is not well defined in front of the bowshock (black and cyan colours). Inside the bowshock it seems that the waves prefer to propagate in the poloidal-toroidal plane, avoiding radial propagation. Together with the position in the dayside magnetosheath, this suggests that in this case the waves propagate more along the magnetosheath than in the cross-magnetosheath direction. Considering the (anti)parallel to the magnetic field propagation found previously, this reflects the draping of the magnetic field lines around the magnetopause.

The parallel propagation can also be observed in the next two panels which are similar with the panels showing the wave vector direction in the previous plot set. The difference is the coordinate system which now is the LMC system. The θ angle made with the radial direction shows a preference towards 90° . The φ angle made with the poloidal-toroidal plane is reduced to angles corresponding to inward propagation ($\theta \geq 90^\circ$).

Description of the B MFA set

Mean Field Aligned (MFA) related parameters are shown in Fig. S2. The top panel is similar with the top panels from the previous discussed plot sets but now the magnetic field time series are represented in the MFA coordinate system. This system has the z axis

aligned with the mean magnetic field vector. The mean magnetic field vector is computed using a boxcar average with the width equal to the sliding step $W/8 = 256$ s used to compute the PSD. The y axis is orthogonal to the mean magnetic field - position vector plane: $\hat{\mathbf{e}}_y^{\text{MFA}} = \hat{\mathbf{e}}_r^{\text{GSE}} \times \hat{\mathbf{e}}_z^{\text{MFA}} / |\hat{\mathbf{e}}_r^{\text{GSE}} \times \hat{\mathbf{e}}_z^{\text{MFA}}|$ and in the inner magnetosphere points roughly in the westward azimuthal direction. The x axis completes the right-handed system: $\hat{\mathbf{e}}_x^{\text{MFA}} = \hat{\mathbf{e}}_y^{\text{MFA}} \times \hat{\mathbf{e}}_z^{\text{MFA}}$, roughly radial in the inner magnetosphere. The x and y directions can substantially deviate from the azimuthal and radial directions in the vicinity of the cusp regions and outside the dipolar field and they take more or less arbitrary directions outside the magnetosphere and in disturbed regions.

The three panels below the time series panel show the power spectral densities for the three components of the magnetic field in the MFA system. In our case, x and y (radial and azimuthal) directions concentrate most of the wave energy, while little energy is contained in the fluctuations parallel to the mean magnetic field. This is made more obvious by the next panel which illustrates the compression ratio C Eq.(18). Most of the magnetic field fluctuations are clearly perpendicular, with the exception of some low frequency fluctuations close to the bowshock crossings and of the waves around 04 UT.

Though the parameters shown in the last three panels are not directly related to the MFA coordinate system, we choose to include them in this set. The wave normal angle and ellipticity were discussed above. The coherence Eq. (13) is equivalent with the polarization degree Eq. (4) only when the noise contribution is isotropic. See e.g. Jones (1979).

Description of the B – density set

This set, illustrated in Fig.S3, shows the parameters related to the electron density fluctuations. Because of time resolution and data availability restrictions of the particle

instruments we derive the electron density from the spacecraft potential using the relations provided by Lybekk et al. (2012). The exact parameters used to derive the electron density were only determined up to 2010. From 2010 on we use the 2010 parameters. This means that the estimated electron density can deviate from the real one. However, the most important density related parameters, the coherence and the phase difference between the magnetic field and density fluctuations are independent on eventual offset or scaling errors in the density. Therefore these parameters are also reliable after 2010. The co- and quad-spectrum values are affected by these errors, but they still describe qualitatively the relation between the magnetic field and the density.

The black line in the top panel shows the magnetic field magnitude smoothed using a sliding window of 1024 s. The red line shows the density. The total PSD of the magnetic field in the next panel is the same as the one in Fig. 1 with the addition of the electron density over-plotted with the yellow line using logarithmic scale. The power spectral density of the density fluctuations computed using the same procedure as for the PSD of the magnetic field is shown in the next panel.

The coherency between the magnetic field fluctuations and the density fluctuations, γ_{Bn} computed from Eq. (13) is plotted in the next panel, with values below 0.6 masked out. The power and polarization masks are applied as well. The coherency is mostly low inside the magnetosheath, but somewhat larger in front of the magnetosheath. Even for these relatively low values, there is still coherent interaction between the field and the particles as reflected by the magnetic field - density phase differences plotted in the panel below. The colours are assigned to the phase difference $\Delta\varphi_{Bn} = \varphi_B - \varphi_n$ as follows: red for opposite phase ($-180^\circ, -135^\circ$) and ($135^\circ, 180^\circ$), blue for in phase oscillations ($-45^\circ, 45^\circ$), yellow for

retarded magnetic field oscillations ($45^\circ, 135^\circ$), and green for retarded density oscillations ($-135^\circ, -45^\circ$). In addition to the power and polarization masks, a mask for coherency $\gamma_{Bn} < 0.5$ was applied. The larger coherency in front of the magnetosheath is reflected in much more stable phase differences across the time-frequency domain as inside the magnetosheath. Here, the field oscillate in opposition to the density, indicating consistent coupling between field and particles. Inside the high polarization time-frequency domains in the magnetosheath, the density fluctuations seem to be retarded from the magnetic field fluctuations, suggesting that the magnetic field drives the density and not the other way around.

The last three panels in this set are the same as those in the *basic parameters* set in Fig. 1.

Description of the Poynting vector direction set

This set, illustrated in Fig. S4, aims to show the direction in which the waves energy flows. The magnetic field time series in the first panel is the same as in Fig. 1. The next panel shows the module of the Poynting vector Eq. (22), with no mask applied. The electric field measured by the Electric Field and Wave Experiment (EFW) (Gustafsson et al., 1997) is downloaded from the CSA at a resolution of 25 vectors per second when available, otherwise a much lower resolution of one vector each 4s is used. One should consider the caveats of the electric field instrument before interpreting these plots. For instance since the end of 2001 only three probes are functional on Cluster 1, same applies to Cluster 3 after mid 2002, and to Cluster 2 after mid 2007. The $\mathbf{v} \times \mathbf{B}$ electric field is removed and no field-aligned electric field is allowed.

The four panels below, showing the direction of the Poynting vector, are similar and use the same coordinate system as for the wave vector direction in Fig. S1. However, in contrast with the wave vector direction, no sign uncertainty exists, and the Poynting vector direction is much more confined indicating a clear anti-sunward flow of the energy in the GSE (θ, φ) right hand side plot and a westward toroidal flow in the left hand side plot. Remarkably, the energy flows in this direction during the entire day, despite increasing distance to the equatorial plane. Data points with the Poynting vector module below $0.5 \mu\text{W km}^{-2} \text{Hz}^{-1}$ were discarded, and power and polarization masks were applied.

The penultimate panel shows the angle between the Poynting vector and the mean magnetic field in the time-frequency domain. Unlike the wave normal angle plotted in Fig. S1, which for the polarized waves inside the magnetosheath keeps a constant (anti)parallel direction to the magnetic field, the Poynting vector changes from anti-parallel near the bowshock to parallel towards the end of the interval reaching in the process large angles to the magnetic field.

Description of the Poynting vector MFA set

The first two panels of this last set of plots shown in Fig. S5, are the same as the first two panels in Fig. S1, and the last panel is the same as the Poynting vector - mean magnetic field angle panel in Fig. S4. The remaining panels show the total power spectral density of the electric field, the components of the Poynting vector in the mean field aligned system defined for the *B MFA* plot set, and the angle between the wave vector and the Poynting vector, reduced to $(0^\circ, 90^\circ)$ due to the sign uncertainty.

Description of the yearly, monthly and daily configuration plots

Yearly overview plots for the entire mission duration are provided, an example being shown in Fig. S6. These are similar with the four years plots but are separated on months and in addition the trajectories in the (e,p) domain are also plotted inside the right hand side colour keys.

A more detailed view of the tetrahedron geometry is offered by the monthly plots. The plot for January 2005 is shown in Fig. S7. The projections of the orbit of the formation barycentre on the three GSE planes allow for a quick estimation of the tetrahedron shape for different magnetospheric regions, while the size of the tetrahedron together with the corresponding colour encoded shape is shown in the fourth panel. To aid linking of the line colour with the (e,p) space and to give a better overview of which regions of the (e,p) space are being visited during the month, the trajectory in the shape space is plotted with white in the colour-key.

The most detailed view of the geometric parameters is given by the daily plots. Fig. S8 is an example for 1st of January 2005. To give an overview of the magnetic field measurements the top panel shows the magnetic field magnitudes measured by the four spacecraft (C1 - black, C2 - red, C3 - green, C4 - blue). The magnetospheric regions in which each spacecraft finds itself are represented by the coloured bars at the bottom of the panel. Top bar for C1, bottom bar for C4. The magnetospheric regions are determined from the Goddard SSCWeb interface <http://sscweb.gsfc.nasa.gov> using IGRF internal and Tsyganenko 89C external model. The six inter-spacecraft distances are presented in the next panel, followed by the geocentric distances for all spacecraft and for the barycentre of the formation. The fourth panel shows the degeneration degree, defined as the radial coordinate in the (e, p) domain: $0 \leq \sqrt{e^2 + p^2} \leq \sqrt{2}$. A small degeneration indicates a

near regular tetrahedron. The degeneration increases as the tetrahedron departs from the regular shape. The bottom left plot shows the trajectory in the (e,p) domain with the time colour coded. The projections of the orbit on the GSE (x,y) , (x,z) , and (y,z) planes and the geocentric distance of the barycentre are shown in the four bottom right plots.

References

- Gustafsson, G., Bostrom, R., Holback, B., Holmgren, G., Lundgren, A., Stasiewicz, K., ... Wygant, J. (1997, January). The Electric Field and Wave Experiment for the Cluster Mission. *Space Science Reviews*, 79, 137-156.
- Jones, A. (1979). On the Difference Between Polarisation and Coherence. *Journal of Geophysics*, 45, 223-229.
- Laundal, K. M., & Richmond, A. D. (2017, March). Magnetic Coordinate Systems. *Space Sci. Rev.*, 206(1-4), 27-59. doi: 10.1007/s11214-016-0275-y
- Lybekk, B., Pedersen, A., Haaland, S., Svenes, K., Fazakerley, A. N., Masson, A., ... Trotignon, J.-G. (2012, January). Solar cycle variations of the Cluster spacecraft potential and its use for electron density estimations. *Journal of Geophysical Research (Space Physics)*, 117, A01217. doi: 10.1029/2011JA016969

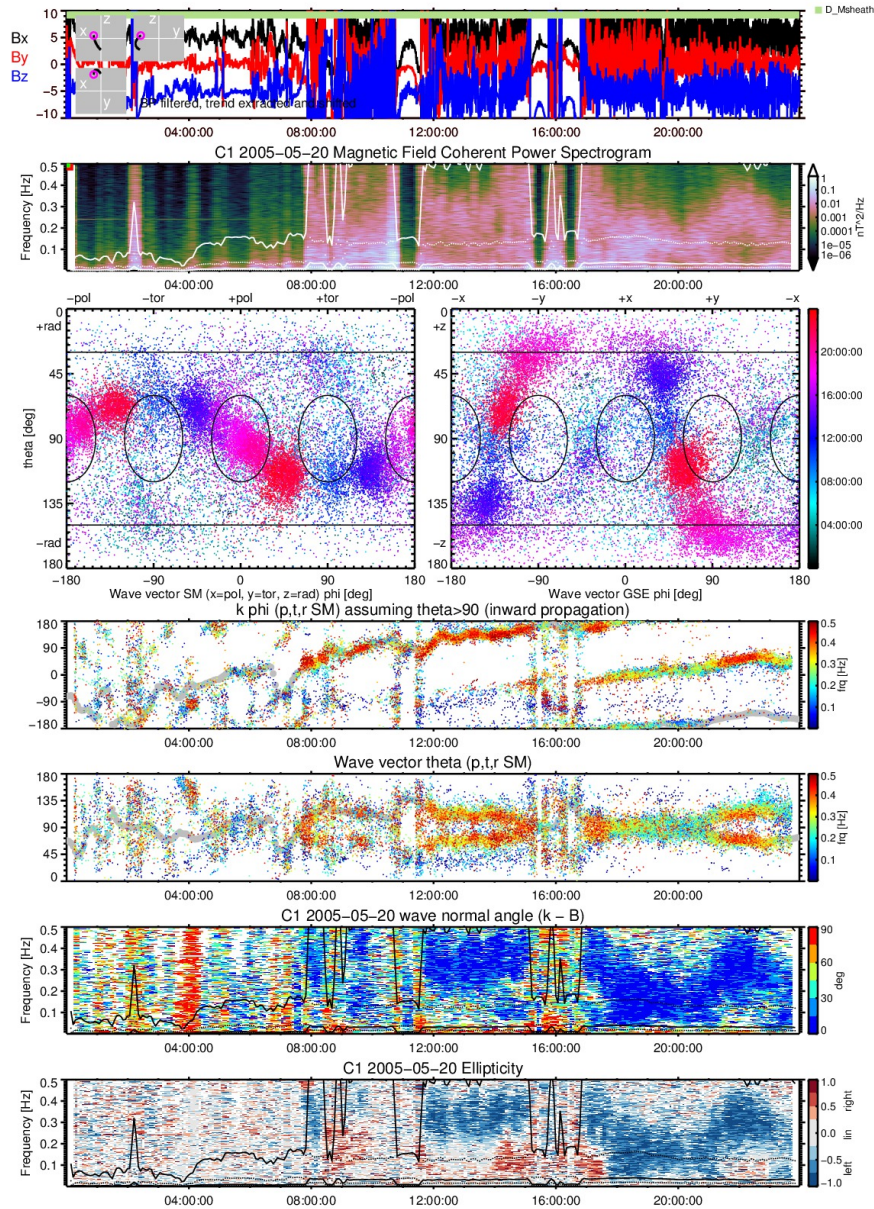


Figure S1. The *wave vector direction* plot set for C1 on 20th May 2005. The top and bottom two panels are the same as in Fig. 1. The second panel shows the PSD of the coherent part of the magnetic field. The third row shows the wave vector orientation in the LMC system (left) and in GSE (right). The two panels below show the wave vector orientation in the LMC system. The mean magnetic field is plotted with the thick grey line.

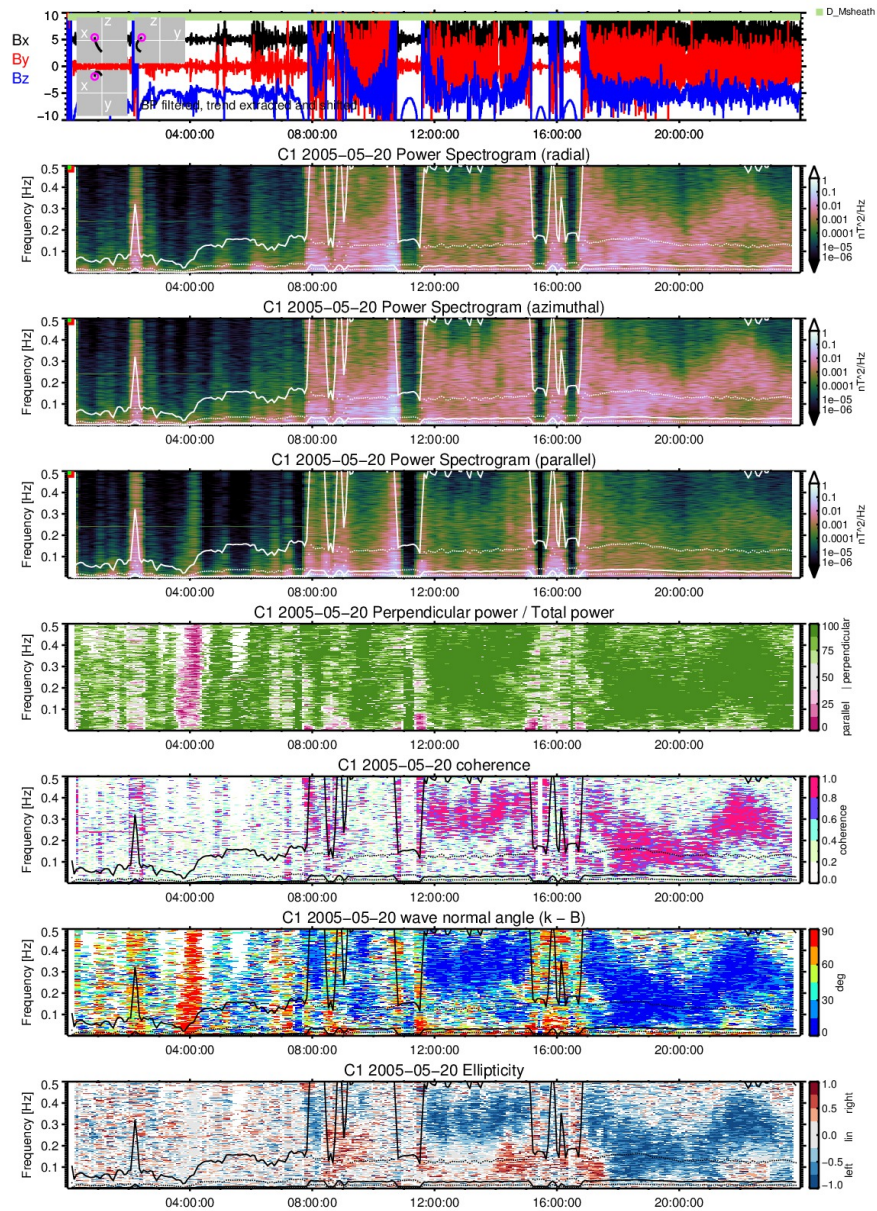


Figure S2. The B MFA plot set for C1 on 20th May 2005. The top panel is similar with the top panel in Fig. 1. The three panels below show the PSD of the magnetic field in the MFA system. The next two panels show the compression ratio and the coherency. The last two panels are the same as in Fig. 1.

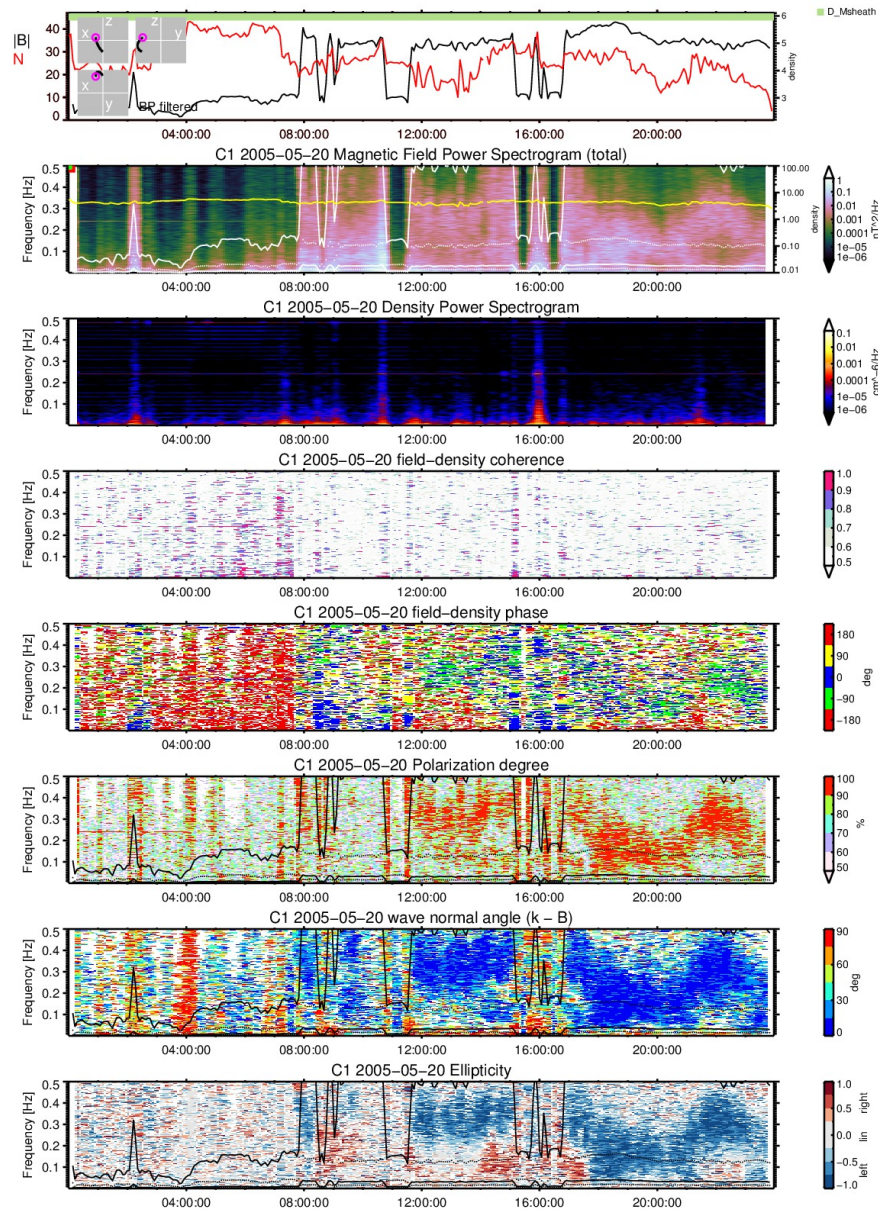


Figure S3. The B - density plot set for C1 on 20th May 2005. The top panel shows the module of the magnetic field (black) and the plasma density (red), both smoothed with a 512 s window; The second panel is the same as the second panel in Fig. 1 with the addition of the plasma density shown by the yellow line; The third panel shows the PSD of the density fluctuations; The fourth panel shows the coherency between the magnetic field and the plasma density fluctuations; The fifth panel shows the phase difference between the magnetic field and the density fluctuations. The bottom three panels are the same as in Fig. 1.

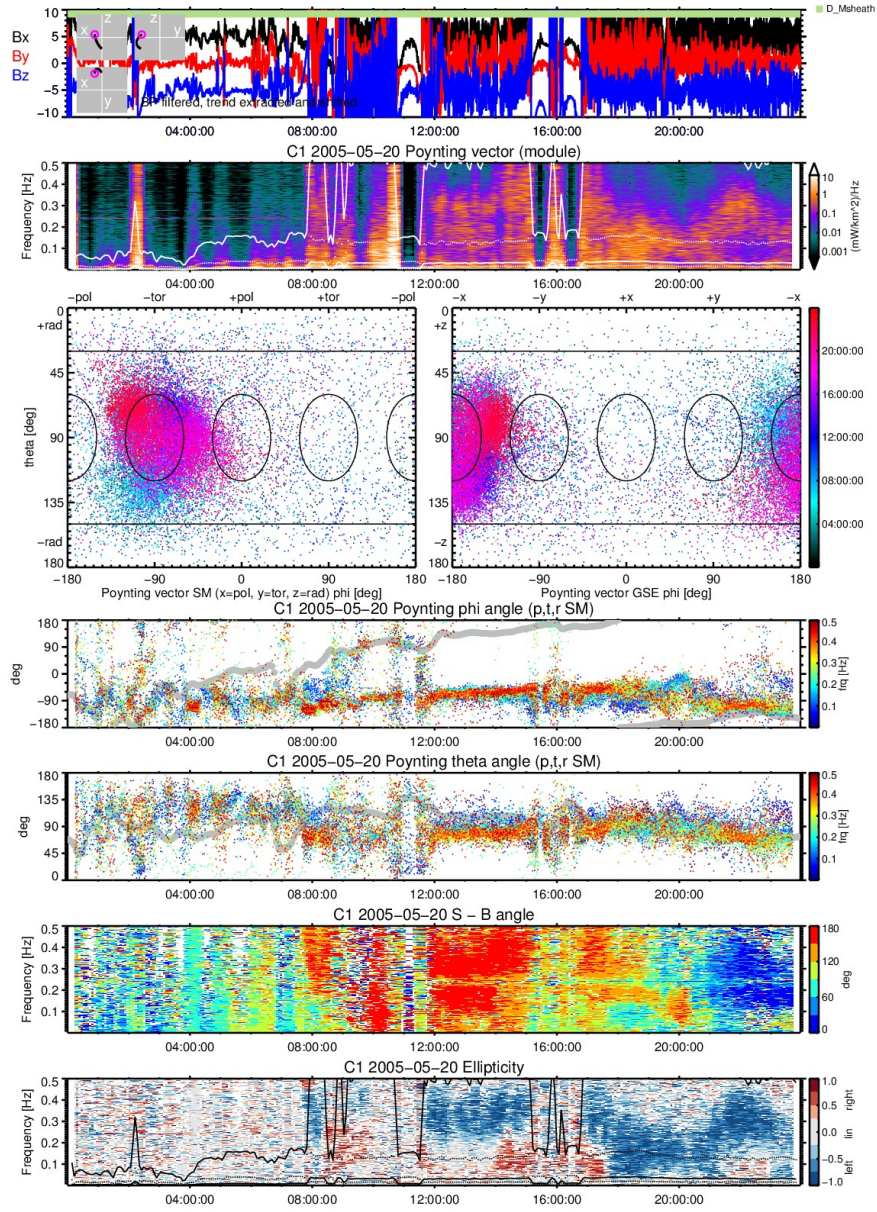


Figure S4. The *Poynting vector direction* plot set for C1 on 20th May 2005. The top and bottom panels are same as in Fig. 1. The second panel shows the PSD of the Poynting vector module and the gyrofrequencies of H, He, and O. The two panels in the third row are similar with those in Fig. S1 but instead of the wave vector direction show the Poynting vector direction. The next two panels show the Poynting vector direction in the LMC system. The second panel from bottom shows the angle between the Poynting vector and the mean magnetic field.

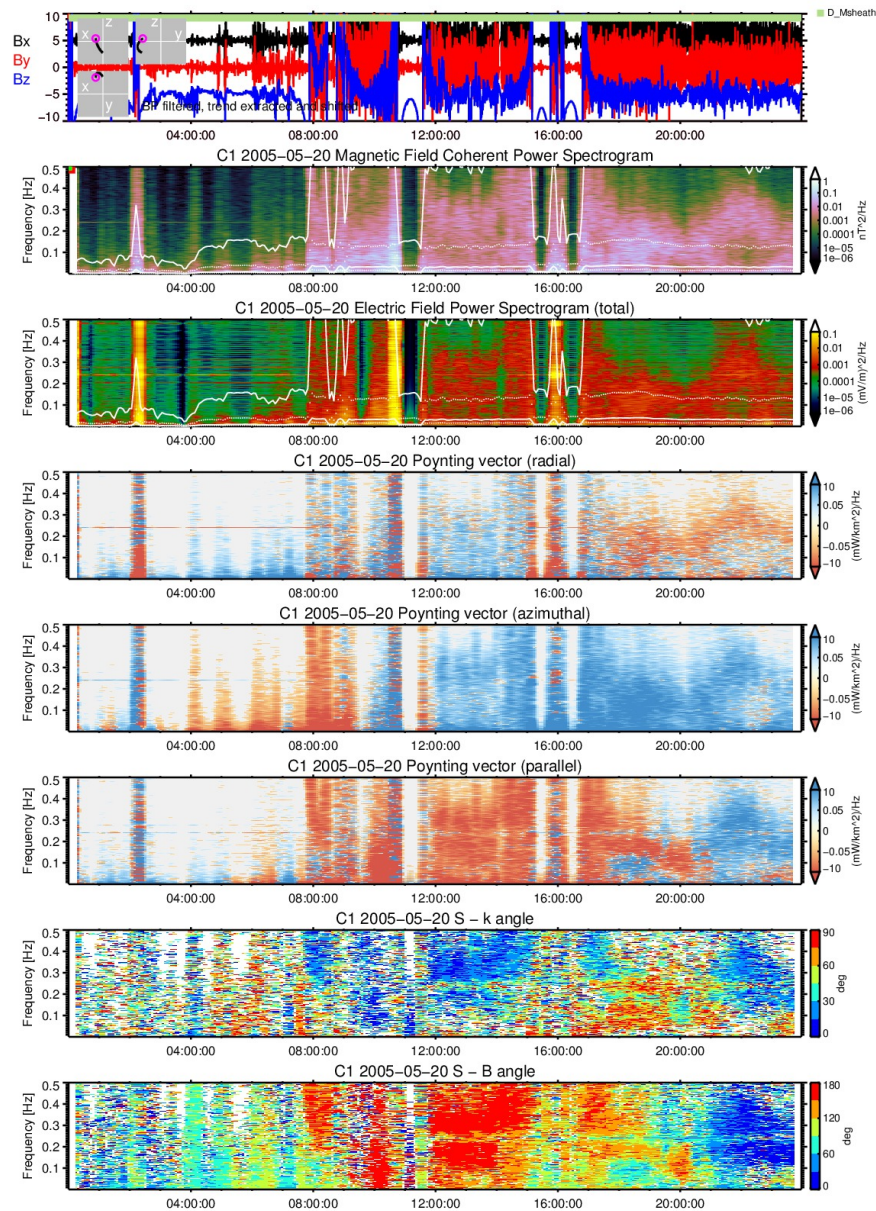


Figure S5. The *Poynting vector MFA* plot set for C1 on 20th May 2005. From top to bottom: Magnetic field in MFA system; PSD of the coherent part of magnetic field fluctuations; Sum of the PSD of the electric field components; Radial, azimuthal, and parallel components of the Poynting vector in the MFA system; The angle between the Poynting vector and the wave vector; The angle between the Poynting vector and the mean magnetic field.

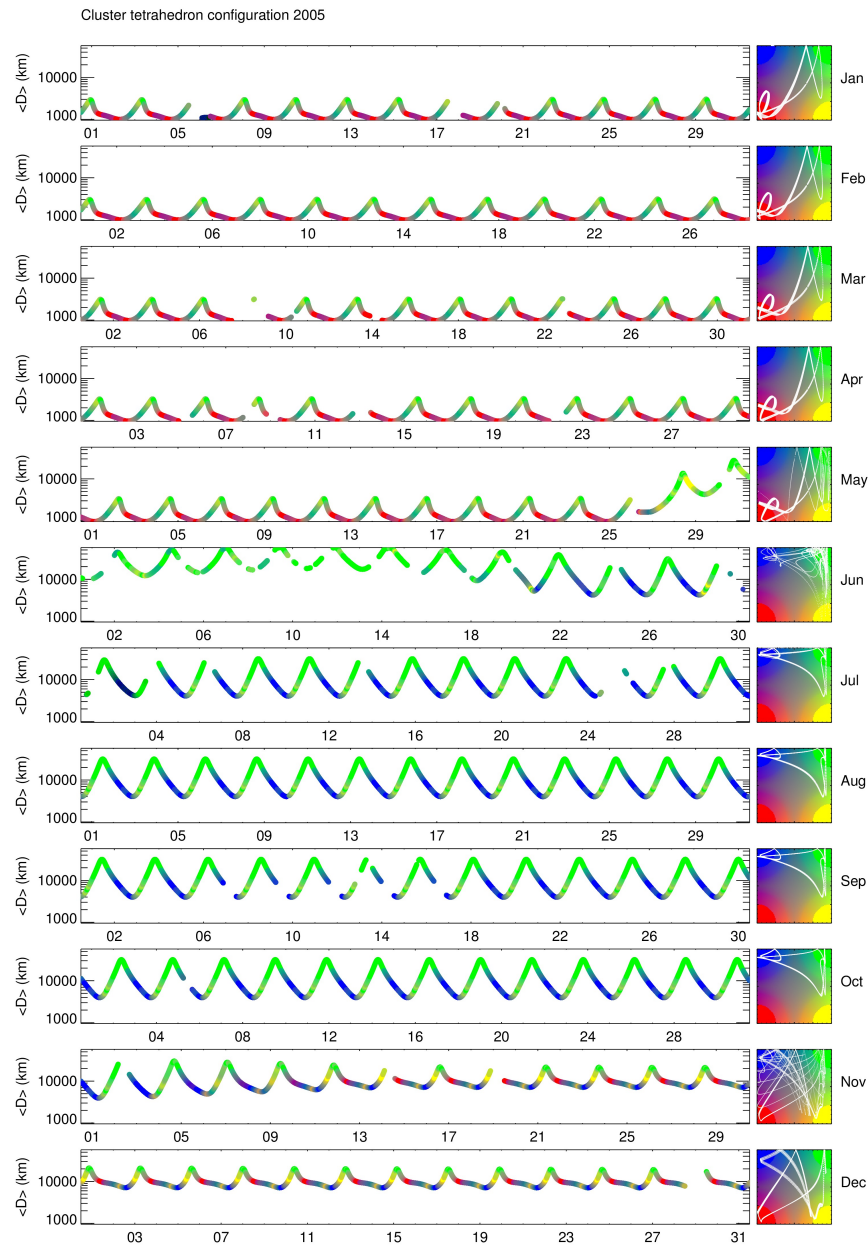


Figure S6. Yearly overview of the mean separation and tetrahedron shape for 2005. The tetrahedron shape is colour encoded and the trajectories in the (e, p) domain are plotted with white in the colour-keys for each month.

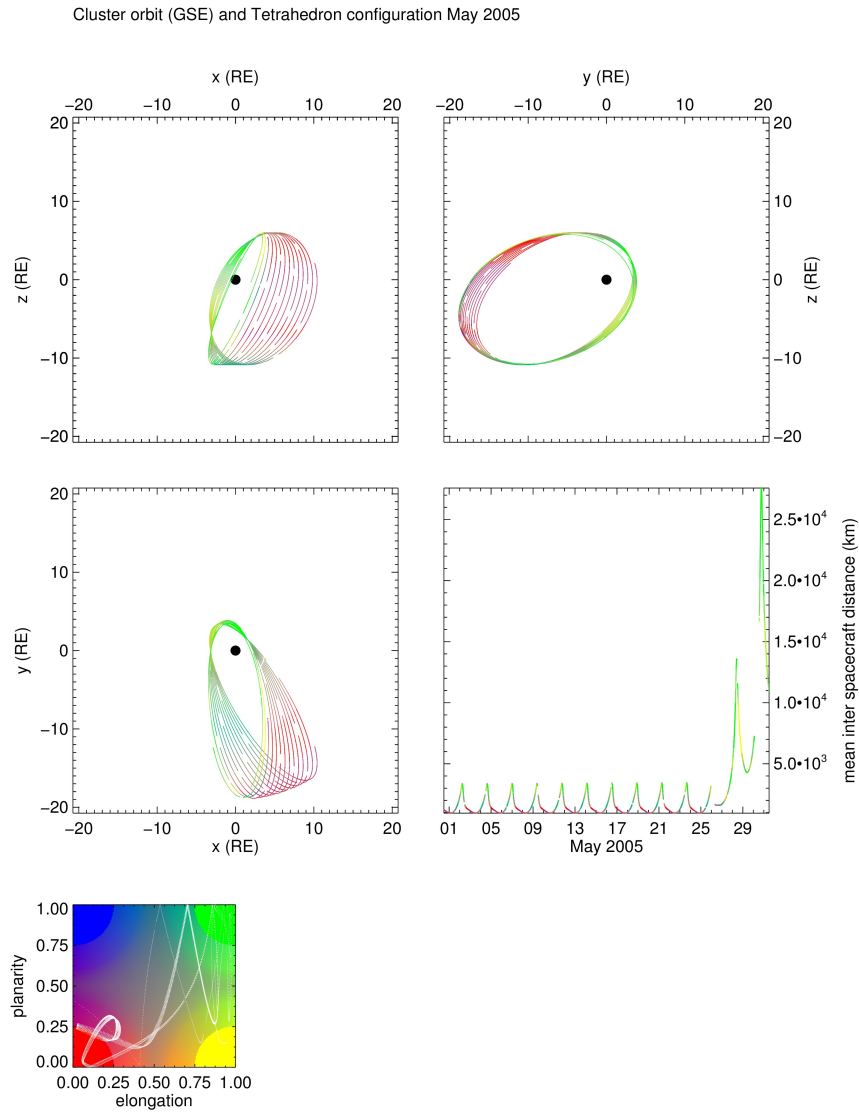


Figure S7. Orbit and geometric parameters of the Cluster tetrahedron during May 2005. The orbits of the formation barycentre are plotted in GSE coordinates and colour coded for the shape with the colour-key in the lower left. The trajectory in the (e,p) plane is shown with white in the colour-key.

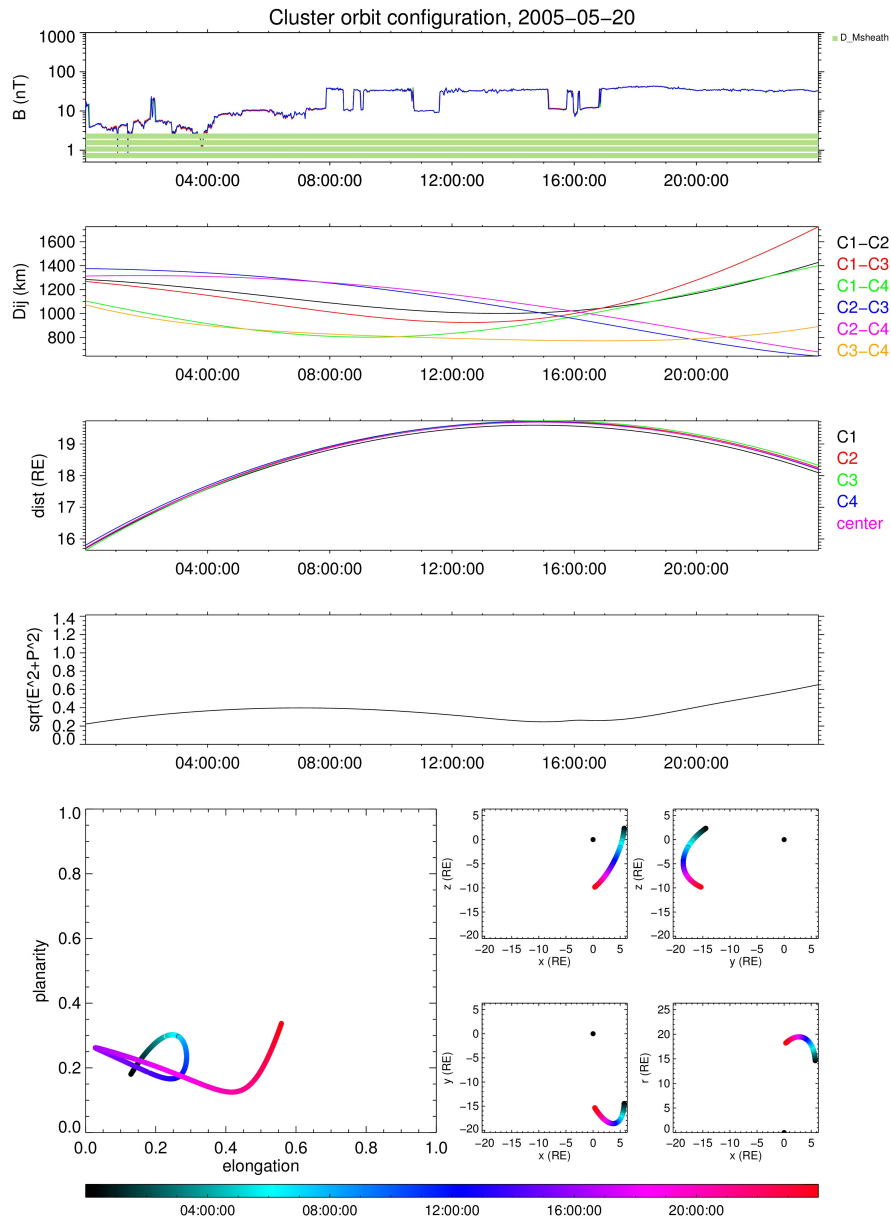


Figure S8. Daily plot for 20th May 2005. From top to bottom: Magnetic field module for the four spacecraft and the magnetospheric regions from SSCWeb. Inter-spacecraft distances. Radial distances for the spacecraft and for the formation barycentre. Degeneration degree of the tetrahedron. Bottom left plot: trajectory in the (e, p) domain, colour encodes the time. Bottom right four plots: barycentre orbit in GSE and barycentre radial distance.

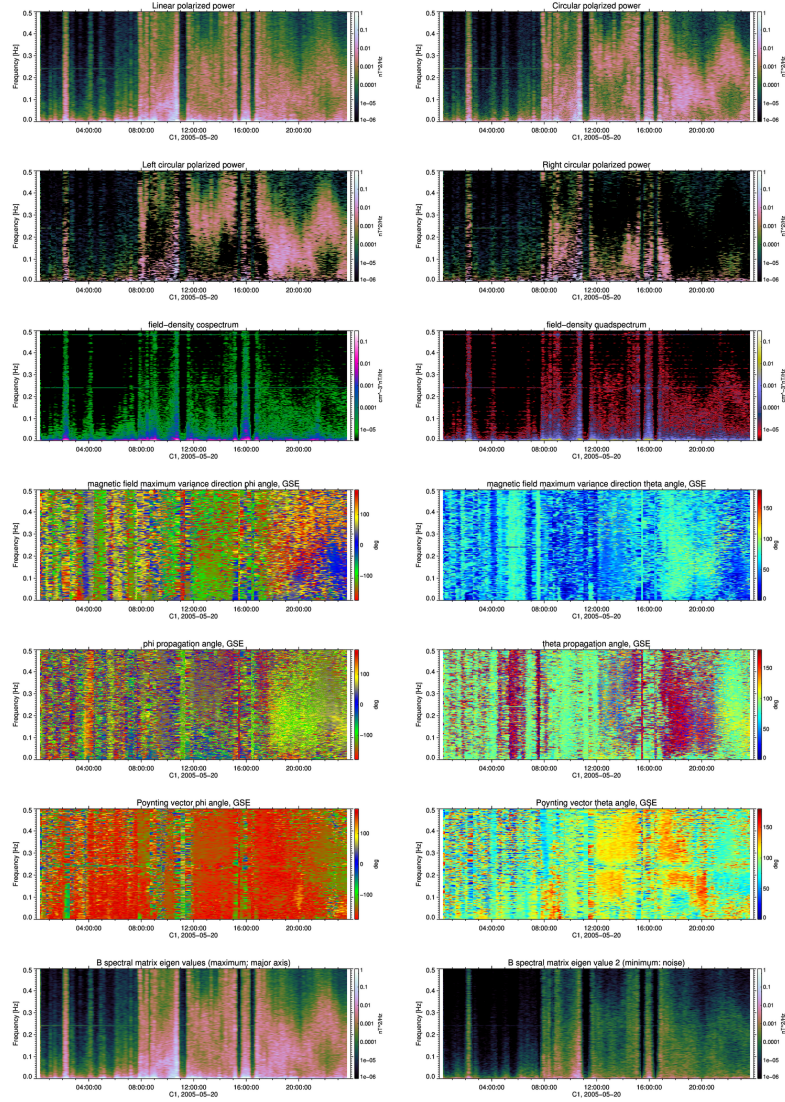
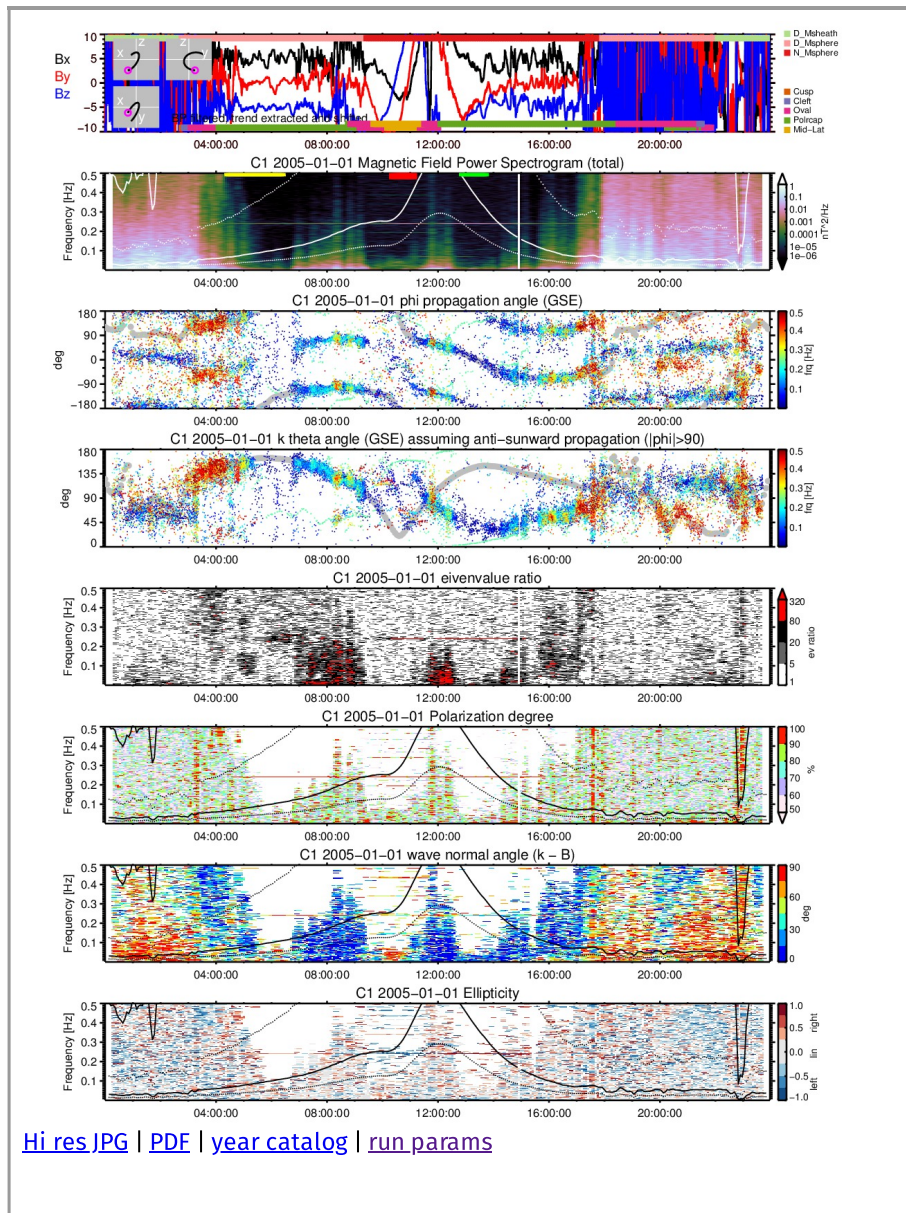


Figure S9. Subset of low resolution quick-view plots for the HDF data archive. No masks are applied. The first panel shows the power spectral density of the linear polarized part of the waves, $P_{\text{lin}} = 2A_{\text{lin}}^2$, with the amplitude of the linear part, A_{lin} from Eq. (16). The PSD of the circular polarized part of the waves is shown next. The circular polarized waves are further divided into the left $P_{\text{left}} = 2(A_{\text{left}}^2 - A_{\text{right}}^2)|_{>0}$ and the right $P_{\text{right}} = 2(A_{\text{right}}^2 - A_{\text{left}}^2)|_{>0}$ polarization in the following two panels. The co- and quad-spectrum of the magnetic field - density fluctuations are shown in the next row. The following three rows show the directions of the magnetic field maximum variance, wave propagation direction, and Poynting vector in GSE coordinates. The last two panels show the maximum and the minimum eigenvalues of the magnetic field spectral matrix.

Cluster virtual observatory for ULF waves

C1 ▾ 2005 ▾ 01 ▾ 01 ▾ Base parameters ▾ go < > [\[data\]](#)



[plot content](#)

Produced by the TUNED-PLAY team

Contact: d.constantinescu@tu-bs.de

Figure S10. The plots section of the CVO.

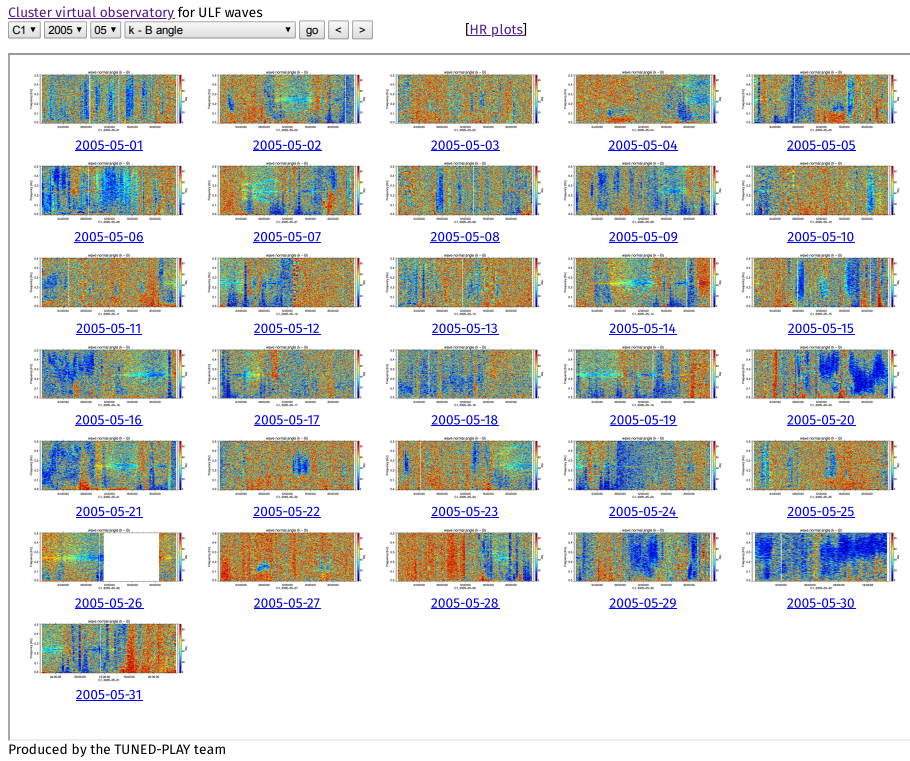


Figure S11. The data section of the CVO.

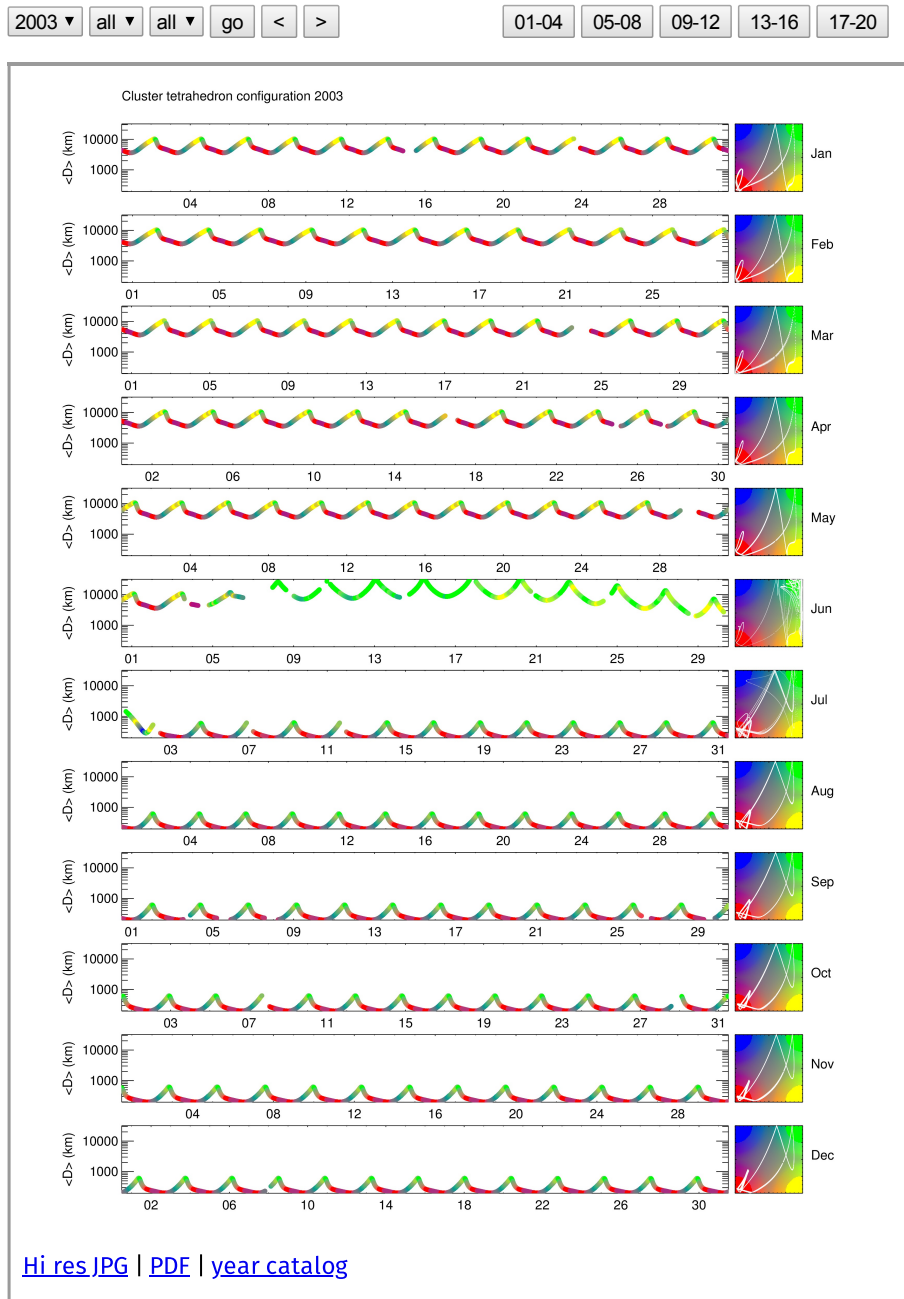
Cluster virtual observatory for ULF waves

Figure S12. The tetrahedron geometry section of the CVO.